Journal of Controlled Release 375 (2024) 537–551

Contents lists available at ScienceDirect

Journal of Controlled Release

journal homepage: www.elsevier.com/locate/jconrel

Cyanocobalamin-loaded dissolving microneedles diminish skin inflammation *in vivo*

Antonio José Guillot [a,b,*], Miquel Martínez-Navarrete [a], Rosa Maria Giner [c], Maria Carmen Recio [c], Helder A. Santos [b], Ana Sara Cordeiro [d,*], Ana Melero [a]

[a] Department of Pharmacy and Pharmaceutical Technology and Parasitology, University of Valencia, Ave. Vicent Andrés Estellés s/n, 46100 Burjassot, Valencia, Spain
[b] Department of Biomaterials and Biomedical Technology, The Personalized Medicine Research Institute (PRECISION), University Medical Center Groningen, University of Groningen. Ant. Deusinglaan 1, 9713 AV Groningen, The Netherlands
[c] Department of Pharmacology, University of Valencia, Ave. Vicent Andrés Estellés s/n, 46100 Burjassot, Valencia, Spain
[d] Leicester Institute for Pharmaceutical, Health and Social Care Innovations, De Montfort University, The Gateway LE1 9BH, Leicester, United Kingdom

ARTICLE INFO

Keywords:
Cyanocobalamin
Vitamin B_{12}
Dissolving microneedles
Skin delivery
Inflammatory skin conditions
Dermatitis
Psoriasis

ABSTRACT

Inflammatory diseases of the skin have a considerable high prevalence worldwide and negatively impact the patients' quality of life. First-line standard therapies for these conditions inherently entail important side effects when used long-term, particularly complicating the management of chronic cases. Therefore, there is a need to develop novel therapeutic strategies to offer reliable alternative treatments. Abnormally high reactive oxygen species (ROS) levels are characteristic of this kind of illnesses, and therefore a reasonable therapeutic goal. Cyanocobalamin, also known as Vitamin B_{12}, possesses notable antioxidant and ROS-scavenging properties which could make it a possible therapeutic alternative. However, its considerable molecular weight restricts passive diffusion through the skin and forces the use of an advanced transdermal delivery system. Here, we present several prototypes of Cyanocobalamin-loaded Dissolving Microarray Patches (B_{12}@DMAPs) with adequate mechanical properties to effectively penetrate the *stratum corneum* barrier, allowing drug deposition into the skin structure. *Ex vivo* penetration and permeability studies noted an effective drug presence within the dermal skin layers; *in vitro* compatibility studies in representative cell skin cell lines such as L929 fibroblasts and HaCaT keratinocytes ensured their safe use. The *in vivo* efficacy of the selected prototype was tested in a delayed-type hypersensitivity murine model that mimics an inflammatory skin process. Several findings such as a reduction of MPO-related photon emission in a bioluminescence study, protection against histological damage, and decrease of inflammatory cytokines levels point out the effectivity of B_{12}@DMAPs to downregulate the skin inflammatory environment. Overall, B_{12}@DMAPs offer a cost-effective translational alternative for improving patients' skin healthcare.

1. Introduction

In the biomedical field, oxidative stress can be considered as two sides of the same coin. On the one hand, it is the cause of multiple pathologies, since it can trigger changes at the molecular level, as a result of DNA base oxidation, lipid peroxidation and protein carbonylation [1]. On the other hand, it can be used as a therapeutic target, to tackle a wide plethora of conditions, from cancer to inflammatory diseases, where it plays a key role in their pathogenesis [2,3]. Thus, as with any other inflammatory pathology, inflammatory skin diseases are associated with oxidative stress damage. Recently, it has been reported that superoxide radical ($O^{2\bullet-}$) produced by an exacerbated NADPH oxidase activity in neutrophils and macrophages may contribute to cytotoxic reactions in the inflammatory microenvironment and modulate the differentiation and proliferation of epidermal fibroblasts and keratinocytes [4,5]. Besides, nitric oxide radical (NO•) has been identified as a biomarker and proinflammatory mediator in abnormal situations [6], being typically increased in conditions such as psoriasis and dermatitis.

Cyanocobalamin, also known as Vitamin B_{12} (B_{12}), is a molecule that possesses antioxidant properties, which are widely described in the literature. These studies have been performed in different scenarios, from *in vitro* to *in vivo*, using cells [7], nematodes [8], and human

* Corresponding author.
E-mail addresses: antonio.guillot@uv.es (A.J. Guillot), sara.cordeiro@dmu.ac.uk (A.S. Cordeiro).

https://doi.org/10.1016/j.jconrel.2024.09.032
Received 12 June 2024; Received in revised form 22 July 2024; Accepted 16 September 2024
Available online 21 September 2024

subjects [9,10]. Overall, different mechanisms have been suggested for this antioxidant function, namely: (a) direct scavenging effect on reactive oxygen species (ROS); (b) indirect scavenging effect through glutathione preservation; (c) modulation of cytokines and growth factors induced by oxidative stress states; (d) reduction of homocysteine-induced oxidative stress; and (e) mitigation of oxidative stress related to advanced glycation end products [11].

The main aim of this study is to effectively deliver B_{12} into the skin structure to treat ROS-related skin conditions, taking advantage of its antioxidant properties. As a consequence of the inherent barrier function that the *stratum corneum* exerts, which is almost inviolable for the vast majority of molecules and drugs, an advanced drug delivery system that can overcome the highly keratinised outer skin layers is needed, to allow drugs to reach the dermal skin structure [12]. Passive diffusion through the skin is a possible pathway, but it is only available when the molecule fulfils certain physicochemical properties, mainly a low degree of ionisation, intermediate partition coefficient, and reduced size (less than 500 Da) [13]. In this sense, B_{12} fails spectacularly, with a considerable molecular weight: 1355 Da [14]. To improve the drug access through the skin, numerous permeability enhancers have been developed over the years, which have shown a sort of success. Nevertheless, they all have certain drawbacks, being far from becoming the ideal solution to this problem. For instance, although they can increase drug fluxes through the skin, chemical enhancers (alkanes, azone, alcohols, surfactants, *etc.*) do not allow skin passage of middle-big sized molecules and localise their effects in the *stratum corneum*, which limits their applicability [15,16]. Physical enhancing strategies using advanced devices (iontophoresis, sonophoresis, electroporation, thermal methods, *etc.*) entail logistic hurdles and an overdue cost-effective ratio that restricts their affordability nowadays, when any aspect is subjected to economic balances [17,18]. Regarding the lipid-based nano-sized systems (liposomes, transfersomes, ethosomes, solid lipid nanocarriers, nanostructured lipid carriers, *etc.*), although they show good results and are considered as one of the most interesting carriers for transdermal and cosmetic applications by far, they are also subjected to long-term stability issues that reduce their translational and commercialisation potential [12].

Microneedling emerged as an advanced strategy that solves most of the above-mentioned problems and has already been proposed for vaccination, local or systemic drug delivery, and sustained release purposes [19]. Micro-array patches (MAPs) stand out for being non-invasive, cost-effective, and efficient devices to increase drug delivery to the skin. MAPs contain micro-sized needle-like projections that mechanically bypass the *stratum corneum* barrier without contacting the nerve endings, allowing the loaded active ingredients to reach the internal skin structure in a painless experience for the user [20,21].

Herein, we report a microneedle-based strategy to optimise local B_{12} delivery into the skin. This approach has been explored to treat systemically its deficiency to date [22]; however, to the authors' knowledge, this is the first time that this combination has been used to treat skin conditions locally. Several combinations of poly(vinyl alcohol) (PVA) and poly(vinyl pyrrolidone) (PVP) were used to produce various prototypes of B_{12}-loaded dissolving MAPs (B_{12}@DMAPs), which release the cargo when the polymers are dissolved after becoming in contact with interstitial skin fluids. The manufactured devices were characterised in terms of morphology, structure, and mechanical properties to choose the most adequate ones. The efficacy of enhancing drug permeability and skin deposition of the preselected prototypes was studied *ex vivo*, while the cytocompatibility was tested in representative skin cell lines, such as fibroblasts and keratinocytes. Finally, the efficacy of B_{12}@DMAPs to diminish skin inflammation was assessed in a delayed-type hypersensitivity *in vivo* murine model, which has barely been explored for MAPs research aimed to treat skin diseases. Moreover, this model allowed us to provide stronger evidence of B_{12} therapeutic efficiency, as it offers objective results and measurements of the findings. This contrasts with previous research, which was supported by PASI (Psoriasis Area and Severity Index) and SCORAD (SCORing Atopic Dermatitis) scores obtained from subjective measurements and perceptions [23–25], commonly used as supportive information only. Besides, we demonstrate the superior benefits of B_{12}@DMAPs over semisolid topical formulations since the obtained data showed that they achieve results as good as those ones obtained by a corticosteroid treatment, which was never clearly obtained by common topical formulations reported in literature [23–25].

The final goal of the developed MAP-device is to offer an alternative for treating inflammatory skin conditions. On one hand, psoriasis and dermatitis are skin conditions with a marked immunoinflammatory nature, chronically affecting around 3 % and 8 % of the world population respectively [26–28], which means millions of patients worldwide. On the other hand, standard therapies based on immunosuppressive drugs, corticosteroids and calcineurin inhibitors entail several problems and limitations, especially when used in long-term treatments. Particularly, when administered systemically, they can lead to important side effects, *e.g.*, liver dysfunction [29], lymphoma risk [30], suppression of the hypothalamic-pituitary-adrenal axis [31], *etc.*, whereas their topical administration might cause skin atrophy, ecchymosis and delayed wound healing, among others [32]. Hence, dermatitis and psoriasis can seem trivial conditions, though lived experience and epidemiological data show that there is a clear need for new treatments to support or even replace the current ones.

2. Materials and methods

2.1. Materials and general reagents

Poly-(vinyl alcohol) (PVA) (MW = 9–10 and 38–50 kDa), poly-(vinyl pyrrolidone) (PVP) (MW = 40 kDa), and oxazolone (purity >99 %) were purchased from Sigma Aldrich (St. Louis, USA). Cyanocobalamin (purity >95 %) was purchased from Acofarma (Madrid, Spain). NaCl, KCl, KH_2PO_4 and $NaHPO_4$ salts were obtained from Scharlab (Santmenat, Spain). HPLC grade methanol (MeOH) and ethanol (EtOH) were obtained from Sigma Aldrich (St. Louis, USA). Ultrapure water (UPW) was obtained by Milli-Q purification system with resistance >18 MΩ cm, and TOC <10 ppb. Acetone (purity 99.9 %) was purchased from ACROS Organics (Geel, Belgium). TNF-α, IL-4, IL-1β and IL-6 ELISA kits were acquired from ThermoFisher Scientific (Waltham, USA).

2.2. Methods

2.2.1. Analytical determination and quantification of B_{12} by high performance liquid chromatography

B_{12} concentrations were determined and quantified by high performance liquid chromatography (HPLC) (PerkinElmer Series 200® HPLC; PerkinElmer, Waltham, MA, USA) using an analytical method described previously [14]. The mobile phase consisted of a mixture of MeOH:UPW (30:70) delivered at a flow rate of 0.7 mL/min. As a stationary phase, a reverse-phase Kromasil® C18 column −5 μm particle size, pore size 100 Å, L x I.D. 150 mm × 4.6 mm- (Dr. Maisch GmbH; Ammerbuch, Germany) was used. To carry out the analytical determinations an injection volume of 50 μL was used, and the UV-detector was set at 360 nm. All analyses were performed at room temperature. The run time for each sample was 5.5 min, and B_{12} retention time was 3.5 min. The analytical method was validated intraday and interday within the concentration range 10–0.04 μg/mL in terms of linearity, precision, accuracy, robustness, and specificity following the recommendations stated in ICH guidelines for validation of a bioanalytical method [33].

2.2.2. B_{12}@DMAPs preparation

Several prototypes of B_{12}-loaded DMAPs were prepared in a one-step manufacturing process by the solvent casting method, using poly (vinyl alcohol) (PVA) and poly (vinyl pyrrolidone) (PVP) as described previously [34–36]. Their quantitative composition is shown in Table 1.

Table 1
Quantitative composition of the different B_{12}-loaded DMAP prototypes developed.

	Composition (% *w*/w)			
Prototype	**PVA 9–10 kDA**	**PVA 38–50 kDa**	**PVP 40 kDa**	**B_{12}**
P1	15	–	5	1
P2	15	–	12.5	1
P3	15	–	20	1
P4	30	–	–	1
P5	–	15	5	1
P6	–	15	12.5	1
P7	–	15	20	1
P8	–	30	–	1
P9	–	–	30	1

Polymers were firstly dissolved in water to prepare stock blends, which were used to prepare the gels at the desired polymer concentration. The gels were mixed with B_{12} until homogeneous. Then, the blends were centrifuged (3500 rpm, 15 min) to remove air bubbles and 0.25 g was poured onto 600 μm height and 200 μm base width polydimethylsiloxane (PDMS) moulds (Micropoint Technologies, Singapore). Following this, the moulds were placed in a positive pressure chamber (Protima® pressure tank, TÜV Rheinland; Cologne, Germany), and a pressure of 3–4 bar was applied for 45 min to fill the cavity of the moulds with the gels. Finally, after drying at room temperature for 24–48 h, DMAPs were carefully demoulded and stored in a dry-seal desiccator for 1 week at least.

2.2.3. *B_{12}@DMAPs characterisation*

The mechanical properties of the different prototypes were studied in terms of morphology, mechanical strength, compression, insertion properties, drug release, and residual water content.

2.2.3.1. B_{12}@DMAPs morphology: SEM imaging. The morphology of DMAPs was observed by scanning electron microscopy (SEM) -EHT 5 kV; WD 10.82 mm-. For this, DMAPs were coated with a conductive gold layer (Q150 RS sputter coater, Quorum Technologies, Lewes, UK) [37]. The length of microneedle projections was measured using ImageJ software (NIH, Wisconsin, USA).

2.2.3.2. Mechanical strength and preliminary insertion properties of B_{12}@DMAPs. Mechanical strength of DMAPs was evaluated using a TA-TX plus Texture Analyser (Stable Micro Systems; Haslemere, UK). DMAPs were visualised before testing using a light microscope (Leica ICC50 HD, Leica Microsystems; Wetzlar, Germany) and then carefully attached to the flat plate of the equipment with the needles pointing downwards. The compression mode was applied with a force of 32 N/array for 30 s to compress the DMAPs against the stainless-steel surface. Finally, DMAPs were again observed under a light microscope to compare the decrease in needle length [38], which was measured using ImageJ software (NIH, Wisconsin, USA). Compression percentage was calculated using Eq. (1):

$$Compression\ (\%) = \frac{h_0 - h_f}{h_0} \cdot 100 \quad (1)$$

Where, *ho* stands for microneedle projections length before compression, and h_f stands for the microneedle projections length after compression. The reported results were obtained as an average of three different batches ($n = 3$).

The insertion depth of DMAPs was preliminarily determined using an artificial skin model. A similar mechanical test set-up was used, but DMAPs were pressed against 8 bound layers of Parafilm® M [39]. The holes created in each layer were counted using a light microscope. The reported results were obtained as an average of three different batches ($n = 3$).

2.2.3.3. In vitro drug release and kinetic release model fitting. *In vitro* release studies were carried out using a method adapted from the literature [40,41]. For that purpose, B_{12}-loaded DMAPs were immersed into 5 mL of PBS pH 7.4 (temperature of 37 °C) in a 12-well plate. To guarantee that sink conditions were maintained throughout the experiment, B_{12} solubility in the receptor media was previously measured by HPLC (12.5×10^4 ppm). At pre-established timepoints (5, 10, 15, 20, 30, 40, 50, 60, 90, 120, 180, and 240 min), 200 μL samples were collected and after every sampling time the subtracted volume was replaced with pre-warmed PBS pH 7.4 to guarantee sink conditions and avoid external auto-concentration, due to the sampling process. The released B_{12} amounts were quantified by HPLC and the cumulative amounts of B_{12} *versus* time were calculated. The reported results were obtained as an average of three replicates ($n = 3$). The total drug amount released was calculated according to the previous determination of drug content and was plotted *versus* time. The release profiles were fitted to the Korsmeyer-Peppas model since it considers the possibility of passive diffusion and polymer erosion phenomena coexisting, as possible drug release mechanisms [42–44]. The possible existence of a burst effect was taken into consideration using the modification proposed in Kim's Eq. [45]. Both kinetic models are described in the Eqs. (2) and (3), respectively:

$$\frac{Mt}{M\infty} = k \cdot t^n \quad (2)$$

$$\frac{Mt}{M\infty} = k \cdot t^n + b \quad (3)$$

Where, *Mt* is the amount released at time *t*, *M*∞ is the maximum amount of drug released, *Mt*/*M*∞ is the fraction of the amount of drug released at time *t*, *k* is the constant that governs the process and explains the characteristics of the system, *n* is the diffusion release exponent, and *b* corresponds to the burst effect parameter. In both models, values of *n* below 0.5 are indicative that the release process is governed by passive diffusion/dissolution; values between 0.85 and 1 show that the process is governed mainly by relaxation/swelling, and intermediate values between 0.5 and 0.85 indicate the existence of both phenomena (anomalous transport) [42,43,45,46].

2.2.3.4. Differential scanning calorimetry. Differential scanning calorimetry (DSC) was carried out using a DSC 214 Polyma (Netzsch; Waldkraiburg, Germany). Temperature scans were performed from 25 to 275 °C at a rate of 10 °C/min [47]. Netzsch Proteus Thermal Analysis 8.0 software (Netzsch; Waldkraiburg, Germany) was used to create baselines and thermograms.

2.2.3.5. Thermogravimetric analysis. Thermogravimetric analysis (TGA) was performed to determine the residual water content of DMAPs after removal from PDMS moulds and one week drying in a dry-seal desiccator. Temperature scans were performed from 25 to 200 °C at a scan rate of 10 °C/min (TG 209 F3 Tarsus; Netzsch, Waldkraiburg, Germany) [48]. Netzsch Proteus Thermal Analysis 8.0 software was used to create baselines and thermograms (Netzsch, Waldkraiburg, Germany). The content of water was quantified by measuring the weight loss from the DMAPs from 0 to 100 °C.

2.2.4. *Ex vivo drug permeation*

Ex vivo drug permeation was tested *ex vivo* using a Franz-diffusion Cell (FDC) setup using 600 μm-dermatomed porcine skin (Micro-line Wagnerd dermatome, Aesculap/Braun; Tuttlingen, Germany) [49]. Briefly, the skin was placed horizontally with the *stratum corneum* facing upwards in-between donor and receptor chambers (effective diffusion area of 1.76 cm^2). To ensure proper insertion of B_{12}@DMAPs, the excised skin was placed onto a foam surface covered with aluminium foil and the donor chamber was strongly attached to the skin using a suitable amount of cyanoacrylate glue (Loctite®, Henkel; Düsseldorf, Germany).

One B_{12}@DMAP was inserted into the skin using a syringe plunger to apply firm pressure for 30 s. To secure the insertion of the DMAPs, they were affixed with Steri-Strip® adhesive bands (3 M-Spain; Madrid, Spain), and finally transferred and correctly placed in the FDC setup. The receptor chamber was filled with 12 mL of receptor media (PBS pH 7.4) and maintained at 32 ± 1 °C under stirring throughout the whole experiment. To guarantee that sink conditions were maintained, B_{12} solubility in the receptor media had been previously measured by HPLC (12.5×10^4 ppm). The donor compartment and the sampling port were covered with Parafilm® M to avoid leakage and solvent evaporation. At pre-established timepoints (0.5, 1, 1.5, 2, 2.5, 3.5, 4.5, 5.5, 6.5, 7.5, 8.5 h), 200 μL samples were collected and after every sampling time, the subtracted volume was replaced with pre-warmed PBS pH 7.4 to guarantee sink conditions. The permeated B_{12} amounts were quantified by HPLC and the cumulative amounts of B_{12} *versus* time were calculated. The reported results were obtained as an average of four replicates ($n = 4$). Maximum flow (Jmax, μg/cm^2/h) and Jmax/dose (cm/h) permeability parameters were calculated by linear regression of the steady state [50].

2.2.5. *Ex vivo B_{12}@DMAPs insertion performance in mice skin and dissolution time*

B_{12}@DMAPs were observed by optical microscopy and then inserted in full-thickness mice skin with thumb-force for 30 s. Then, they were removed after 2, 4, 8 and 12 h post-insertion and imaged to appreciate the dissolution of microneedle projections [47]. In addition, the cargo deposition within the skin structure 2, 4, 8, and 12 h post-insertion was visually evaluated based on the red colour intensity of B_{12} (Juision 2 K camera).

2.2.6. *In vitro compatibility in fibroblasts and keratinocytes cell lines*

Cytotoxicity was evaluated using L929 fibroblasts (passages 50–60) and HaCaT keratinocytes (passages 51–54) [51]. Cells were cultured in separated flasks (75 cm^2) in Modified Eagle's medium (MEM) supplemented with 1 % (*v*/v) GlutaMax™ (Gibco, Invitrogen, USA) and Dulbecco's modified Eagle's medium high glucose (4.5 g/L) (HyClone, Logan, UT) respectively, containing both 10 % of foetal bovine serum (Gibco, Invitrogen, USA), 1 % (v/v) of L-glutamine, 1 % (v/v) of nonessential amino acids, 100 IU/mL of penicillin, and 100 mg/mL of streptomycin (HyClone, Logan, UT). Both cell lines were cultured at 37 °C, 5 % CO_2 and 95 % relative humidity. The medium was changed every other day and cells were subcultured before reaching confluence (60–70 %).

Prior to each test, cells were harvested and diluted at a density of 1×10^5 cells/mL. The cells were then seeded in separated 96-well plates for 24 h (0.2 mL per well). After the cell attachment to the wells, the medium was discarded, and cells were washed with 200 μL of PBS pH 7.4. Cells were exposed to different concentrations −150, 75 and 30 mg/mL-of PVA (MW 9–10 kDa), PVA (MW 38–50 kDa) and PVP (MW 40 kDa) with 1 % *w*/w of B_{12} for 24 h. Afterwards, cells were washed twice with PBS pH 7.4 and the number of viable cells were quantified using the CellTiter-Glo® assay according to the protocol specified by the manufacturer [52]. For that, 10 μL of CellTiter-Glo® reagent and 10 μL of PBS pH 7.4 were added to each well for 15 min. Luminescence was measured using a Synergy H1 microplate reader (Biotek, Vermont, USA). Untreated cells and SDS 1 % (w/v) were used as negative and positive controls, respectively. The reported results were obtained as an average of three independent assays ($n = 3$).

2.2.7. *In vivo delayed-type hypersensitivity murine model*

Swiss-CD1 female mice (4–6 weeks old) were acquired from Harlan Interfauna Iberica (Barcelona, Spain) and stabled in SCSIE facilities (University of Valencia). The housing conditions and the *in vivo* procedures were approved by the Institutional Ethics Committee of the University of Valencia and regional government in accordance with the guidelines established by the European Union on Animal Care and the principles of Helsinki declaration (2023-VSC-PEA-0064). Fig. 1 illustrates the delayed-type hypersensitivity (DTH) *in vivo* murine model timeline carried out.

2.2.7.1. *Induction of the delayed-type hypersensitivity.*

Briefly, abdominal areas were shaved and sensitised with a single topical application of 150 μL oxazolone (OXA) (3 % w/v) dissolved in acetone (day 0). Afterwards, mice backs were shaved and challenged with a second administration of 150 μL of OXA (1 % w/v) [53]. Straightaway, the treatments were applied (day 6). Mice were randomly assigned to five different groups prior to the experiments as compiled in Table 2 ($n = 6$). In case of DMAPs treatment, prior to the insertion of DMAPs devices, the skin was hydrated with PBS pH 7.4 and then DMAPs were secured to the skin as described previously [34].

2.2.7.2. *Bioluminescence imaging.*

Using a IVIS Lumina X5 bioluminescence imaging system (PerkinElmer, Waltham, USA), bioluminescence imaging (BLI) was performed 24 h after OXA challenge (day 7). For this, an intraperitoneal injection of luminol sodium salt (200 mg/kg, 0.2 mL) was administered to mice. Animals were then anaesthetised 20 min after luminol injection by isoflurane inhalation and imaging was performed [53]. Regions of interest (ROI) were precisely selected on the DMAPs insertion sites, and the total photon emission was subsequently measured. After BLI study, mice were killed by cervical dislocation under appropriate anaesthesia and analgesia conditions.

2.2.7.3. *Histological study.*

Skin biopsies were obtained using a biopsy punch and carefully divided for further studies. For the histological study they were prior fixed in paraformaldehyde 4 % (w/v). Then, samples were washed, dehydrated, paraffin-embedded and cut in 10 μm-thickness sections. Haematoxylin-eosin (H&E) and Masson trichrome (MT) collagen stains were used to visualise the anatomical and morphological changes [54,55]. Epidermal and collagen deposition thickness were measured using ImageJ software (NIH, Wisconsin, USA) in 20× magnification images [56]. A total of 3 samples from 3 different mice from each group were initially analysed by a blinded investigator.

2.2.7.4. *Inflammatory cytokines detection and myeloperoxidase activity quantification.*

Skin biopsies were homogenised by freezing with liquid nitrogen followed by pulverisation. Then, they were embedded in a lysis buffer as described previously. Enzyme-linked immunosorbent assays (ELISA) commercial kits were used to quantify IL-1β, IL-6, TNF-α and IL-4 as inflammatory cytokines. Quantification was performed according to the instructions provided by the manufacturer (ThermoFisher Scientific, Waltham, USA) [57]. Specifically, for myeloperoxidase (MPO) activity quantification, 5 μL of tissue homogenates were mixed with 195 μL of PBS pH 7.4, 20 μL of Phosphate buffer pH 5.4, 20 μL of hydrogen peroxide 0.052 % (w/v) and 20 μL of tetramethylbenzidine (TMB) 15 mM in dimethylformamide (DMF) 8 % (w/v) and incubated at 37 °C. The reaction was stopped after 10 min with 100 μL of sulfuric acid 2 N. Finally, absorbance was measured at 450 nm with a plate reader (VICTOR^3 Multilabel Plate Reader; PerkinElmer, Waltham, USA). The reported results were obtained as an average of three different mice ($n = 3$).

2.3. *Statistical analysis*

Data processing was performed using Microsoft Excel 2016® (Redmond, WA, USA) and SPSS version 22.0® (IBM Corp., NY, USA). Data are expressed as the mean ± standard deviation (SD) unless otherwise stated. Assumptions of normality and homogeneity of variances were considered in all analyses. Statistical analysis was carried out using Student's *t*-test for simple comparisons, and one-way ANOVA followed by Tukey post-hoc test.

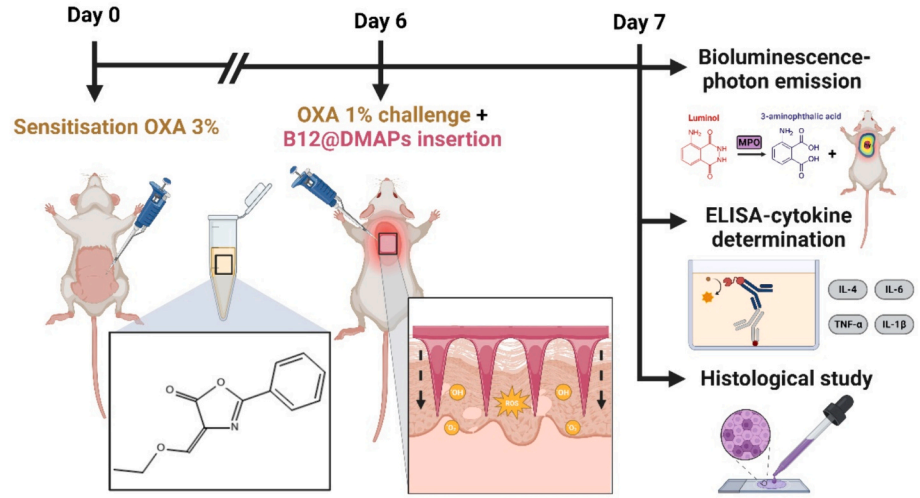

Fig. 1. Illustration of the delayed-type hypersensitivity (DTH) murine *in vivo* model. Briefly, animals are sensitised with a single topical application of oxazolone (OXA) 3 % (w/v) in the abdominal area. Six days after mice are challenged with a second topical administration of oxazolone 1 % (w/v) in the back area to develop a cutaneous inflammation. Afterwards, B_{12}@DMAPs devices are applied for 24 h. Them, MPO-related activity is measured by bioluminescence-photon emission and animals are sacrificed according to the standard protocols of animal care. Finally, skin biopsies are obtained to determine levels of inflammatory cytokines and histological changes.

Table 2
Animal groups in the delayed-type hypersensitivity murine model (n = 6).

Group	Condition	Information
OXA	Negative control	Non-treated after OXA challenge
Healthy	Naïve	Unchallenged
DEXA	Positive control	Dexamethasone treatment: 1.25 μg/μL; 150 μL; DEXA dissolved in EtOH:UPW (7:3)
B_{12}@DMAPs	B_{12}-loaded DMAPs	Prototype P9
Blank	Unloaded DMAPs	Prototype P9

3. Results and discussion

3.1. B_{12}@DMAPs characterisation

DMAPs are the most representative exponent of an attractive group of technologies that bypass biological barriers and deliver drugs to target tissues or close to blood supply. They standout for facilitating transdermal drug delivery particularly for BCS class III and IV molecules [58]. Cyanocobalamin (B_{12}), which falls into class III group due to its high solubility but low permeability [59], is an excellent candidate for DMAP-based delivery because of its easy incorporation in a water-based matrix. In fact, several DMAP-based systems have been developed for local, intradermal and transdermal delivery of highly soluble drugs such as lidocaine [60], insulin [61], and siRNA [62].

Aqueous B_{12} dispersions with different biocompatible polymers were used either alone or in combination to prepare B_{12}-loaded DMAP prototypes through the solvent casting, as detailed in previous works [34–36]. For this purpose, PVA (9–10 and 38–50 kDa) and PVP (40 kDa) were selected due to their good biocompatibility previously shown in polymer-based biomedical devices [63]. Moreover, several prototypes based on different polymer compositions (polymers proportion and concentration) within the usual range to prepare polymeric-based DMAPs were developed since it can influence key properties that determine their success like mechanical strength, insertion capacity and cargo release, as previously reported. However, one of the formulations (P8) did not produce optimal DMAPs, since it consisted in an excessively viscous polymer blend (30 % *w*/w of high-molecular weight PVA), which did not allow a successful gel pouring into the needle moulds after the application of a positive pressure of 3–4 bar. The rest of the formulations produced homogeneous polymer mixtures and the resultant DMAPs exhibited sharp needle tips upon visual examination under light microscope and SEM imaging (Fig. 2A). The pyramidal needle shape is a result of the PDMS mould type used in this experiment. This mould design was specifically chosen for its ability to improve drug loading. Moreover, pyramidal-shaped needles can maintain their shape after insertion and increase the drug release rate by increasing the contact surface with skin [64,65]. The mechanical strength and preliminary insertion were subsequently tested.

The ability of DMAPs to effectively pierce the skin is crucial to their efficacy because they must completely penetrate the *stratum corneum* to deliver their cargo. Mechanical strength evaluation was carried out to determine the capability of B_{12}@DMAPs to resist the applied compression force when inserted into the skin. The percentage of length reduction of the needles on the arrays after the application of a force similar to manual compression force (32 N/array) was determined to estimate the mechanical strength of the different prototypes [39]. The compression of DMAPs produced significant needle bending height reduction in all cases ($p < 0.05$) (Fig. 2B). However, the specific percentage of needle compression strongly depended on polymer combination and concentration (Fig. 2C).

DMAPs prepared using only PVP as a polymer (P9) exhibited one of the maximum needle height reductions (>30 %) and needle deformation, as previously reported [35]. In the same way, the PVA (9–10 kDa)-based prototype (P4) showed considerable needle height reduction (>40 %). In contrast, prototypes formulated with a combination of PVA and PVP (P1-P3 and P5-P7) exhibited less compressive behaviour. PVA 9–10 kDa-based DMAPs did not show any difference among the different polymer proportions. Moreover, PVA 38–50 kDa-based prototypes were more resistant to compression, especially when the PVP concentration increased (P7). Specifically, the compression percentage of the P7 prototype was significantly lower than the other DMAPs prototypes ($p < 0.05$), except for the polymer combinations (P5 and P6) (Fig. 2D). This finding agrees with previously reported results where the combination of PVP and PVA improved the mechanical properties of the formulation, which was attributed to the hydrogen-bond interactions between hydroxyl groups of PVA and carbonyl groups of PVP [35,63,66]. Nevertheless, the crucial feature microneedle-based systems must satisfy is the insertion performance. For that, Parafilm® M was used as a validated

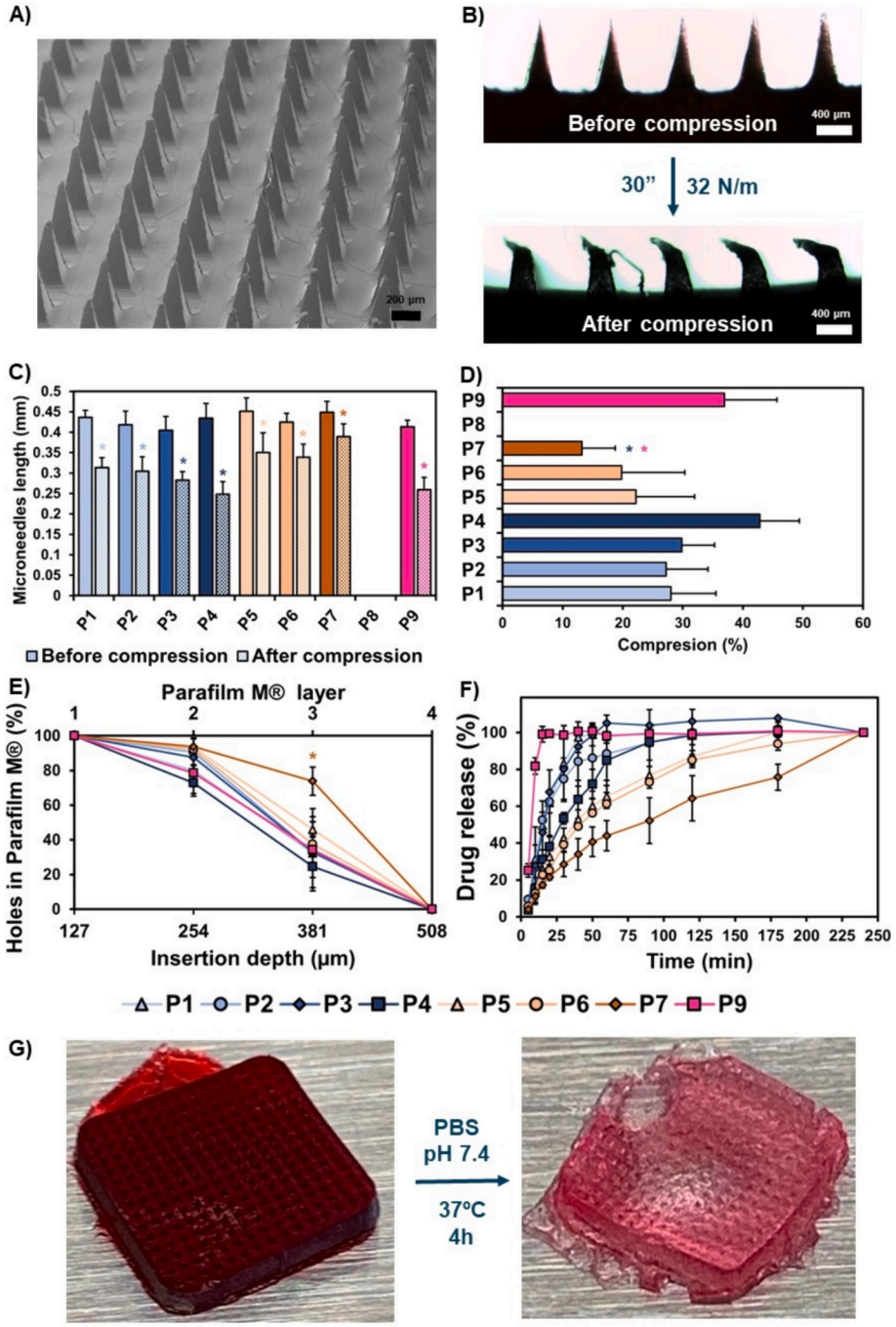

Fig. 2. a) SEM image of the B_{12}@DMAPs (prototype P9). Scale bar: 200 µm; **b)** Optical microscopy images of B_{12}@DMAPs (prototype P9) before and after 30 s compression (32 N/m). Scale bar: 400 µm; **c)** Microneedle tips length (mm) before and after 30 s compression (32 N/m). P8 spot remains empty since functional DMAPs were not formed. * denotes statistically significant differences between pre- and post-compression length ($p < 0.05$); **d)** Compression percentage of microneedle tips length after 30 s compression (32 N/m). P8 spot remains empty since functional DMAPs were not formed. * denotes statistically significant differences in comparison with other prototype ($p < 0.05$); **e)** Insertion percentage from different DMAP prototypes in Parafilm® M artificial skin model. Results are expressed as mean ± SD ($n = 3$); **f)** B_{12} release profiles from different DMAP prototypes. Results are expressed as mean ± SD (n = 3); **g)** Cyanocobalamin-loaded PVA (38–50 kDa)-based DMAPs before and after dissolution in PBS pH 7.4 at 37 °C after 4 h dissolution.

artificial skin surrogate for insertion studies of microneedle-based devices, as previously described [39]. Although it is less structurally complex than excised skin and bioengineered artificial tissues, Parafilm® M provides sufficient hydrophobic *stratum corneum*-like properties, serving as a rapid quality control test [67]. The results of the insertion studies were in solid agreement with the mechanical strength studies (Fig. 2E). P7 prototype, which showed superior mechanical strength, penetrated until the third Parafilm® M layer in a higher significant proportion ($p < 0.05$) than the other prototypes. However, the other DMAPs reached the same penetration depth (>80 % needle length), since the mean thickness of a Parafilm® M layer is 126 ± 7 µm, indicating that microneedles were inserted up to 378 µm of the total height. These values were similar to previous studies that focused on the insertion of other polymeric DMAPs into human skin [68], and indicate that, even though the P7 prototype possesses higher mechanical resistance against compression, all of them have sufficient mechanical

strength for being inserted and successfully overcome the outer skin layers responsible for skin barrier function.

The other key aspect of the present study is the drug release pattern that the different prototypes exhibit. Specifically, the selected DMAPs prototype for *in vivo* testing must be able the release B_{12} in the shortest time, to avoid removal of the device by mice motion after application. The use of different polymers to produce DMAPs led to different mechanical strength properties as showed, but also physicochemical behaviour that influence the drug release process as a consequence of the different solubility of the polymers (Fig. 2F). PVP-based formulation (P9) showed the fastest drug release, at least 2.5-fold faster than PVA 9–10 kDa-based DMAPs (P1-P4) and around 8-fold faster than PVA 38–50 kDa-based prototypes (P5-P7), based on Kd values from the Korsmeyer-Peppas kinetic model (Table 3**; Tables S1-S16 Supplementary material**) [42,43]. The most probable reason for this could be that PVP is much more soluble in water than PVA [69], which facilitates polymer diffusion into the release media and, therefore, DMAP disintegration. In the same trend, PVA 38–50-based DMAPs (P6-P8) showed a slower release than PVA 9–10 kDa-based ones (P1-P4), since the increase of molecular weight limits polymer dispersibility [70]. In addition, from the Kd results it can be corroborated that PVP/PVA combination increases the mechanical features of the resulting DMAPs, as Kd values from PVP/PVA-based DMAPs are significantly superior to those of the single polymer-based prototype (P1-P3 *vs* P4, and P5-P7 *vs* P9). At the end of the release studies, PVA 38–50 kDa-based prototypes were the only ones that preserved the polymeric matrix (Fig. 2G), denoting a polymer swelling alternative release mechanism to diffusion/dissolution. The "*n*" parameter of this kinetic model has been evaluated in depth, to better understand the underlying release mechanism (Table 3). As expected, only P5-P7 prototypes showed an "*n*" value $\geq$0.5, confirming the non-fickian combined release mechanism [71], while the others followed a fickian release mechanism ($n < 0.5$). Finally, the existence of a burst effect [72], particularly in the P9 formulation, was discarded fitting the release data to the Kim model and obtaining an absolute zero value for the "*b*" parameter.

3.2. Differential scanning calorimetry and thermogravimetric analyses of B_{12}@DMAPs

B_{12}@DMAPs were characterised by DSC to study the interactions between polymers and ensure that polymers did not form a heterogeneous blend that could be responsible for the different release profiles observed. As it can be seen in Fig. 3A, depending on the main component present in the formulation, the thermograms showed a particular profile. The PVP-based prototype (P9) showed a characteristic signal in the 50–150 °C range [73], caused by the amorphous nature of PVP [74]. The integration of this wave in the PVA/PVP-based formulations confirmed the integration of both polymers in a homogeneous mixture, suitable for biomedical and bioengineering applications [74]. Additionally, PVA 38–50 kDa-based formulations (P5-P7) exhibited a characteristic peak at 210–220 °C, attributed to the melting of crystalline PVA [75]. Overall, the most promising prototypes from the previous studies were P3, P7 and P9. Specifically, the fast B_{12} release provided by P9, the high insertion and strong mechanical properties of P7, and the intermediate behaviour of P3 explain this selection.

Following removal from the PDMS moulds (after 48 h drying), the arrays exhibited a discrete flexible behaviour. However, one week later, they were completely resistant to deformation and achieved their full strength and insertion properties. Therefore, all further studies were performed after storing the arrays in the desiccator for 7 days. The most probable reason for this behaviour is that after 48 h the drying process was still incomplete, conferring a certain degree of flexibility to the arrays, as final polymer chain interactions were not completely established, and polymers were more sensitive to heat degradation. This was monitored by TGA analysis of the selected prototypes (P3, P7 and P9) up to 1-week post-manufacturing, while DMAPs were stored in a dry-seal desiccator to eliminate any residual water content (Fig. 3B). Results showed that B_{12}@DMAPs lost a higher percentage of weight 48 h after production, compared to 7-day dried devices. Particularly, a temperature of 200 °C produced a weight loss of around 12–14 % and 7–9 %, respectively. Moreover, the partial weight lost at 110 °C corresponding to residual moisture content differed according to the drying time, decreasing from 4 % to 2 %, which was the maximum water content observed experimentally [48].

Table 3
B_{12} release parameters from the different DMAPs prototypes fitted to Korsmeyer-Peppas and Kim kinetic models of drug release. All results are expressed as mean ± SD ($n = 3$).

	Korsmeyer-Peppas		Kim		
	Kd	n	Kd	n	b
P1	28.05 ± 8.92	0.27 ± 0.06	28.05 ± 8.92	0.27 ± 0.06	0 ± 0
P2	24.09 ± 7.05	0.29 ± 0.03	24.09 ± 7.05	0.29 ± 0.03	0 ± 0
P3	25.87 ± 3.64	0.28 ± 0.01	25.87 ± 3.64	0.28 ± 0.01	0 ± 0
P4	12.79 ± 2.61	0.40 ± 0.03	12.79 ± 2.61	0.40 ± 0.03	0 ± 0
P5	7.31 ± 0.65	0.50 ± 0.02	7.22 ± 0.72	0.50 ± 0.02	0 ± 0
P6	7.07 ± 1.05	0.50 ± 0.02	7.07 ± 1.05	0.50 ± 0.02	0 ± 0
P7	3.45 ± 1.57	0.62 ± 0.06	3.45 ± 1.57	0.62 ± 0.06	0 ± 0
P9	59.22 ± 1.43	0.11 ± 0.01	59.22 ± 1.43	0.11 ± 0.01	0 ± 0

3.3. B_{12}@DMAPs ex vivo permeability/insertion and in vitro compatibility

According to the previous results, P3, P7 and P9 prototypes were considered as representative formulations of slow, intermediate, and fast drug release, respectively. Therefore, their *ex vivo* permeability was determined to establish a possible release/permeability corelation. For that purpose, 600-μm thickness skin was used to measure the specific B_{12} permeation into the dermal layers. Although B_{12}@DMAPs provided an effective diffusion of B_{12} through the skin in comparison to an aqueous B_{12} solution, which provided negligible drug absorption, no differences between prototypes were observed in terms of cumulative drug amount permeated and permeability parameters, surprisingly (Fig. 4A and Table 4). Several factors like insertion depth, drug release rate or *stratum corneum* barrier nullification could motivate these results. First, the *in vitro* release and FDC experimental setups differ considerably, since aqueous volume is considerably lower in FDC experiments. Second, insertion depth differences can play a crucial role and, for instance, even though P9 showed a faster B_{12} release in the *in vitro* test, the deeper insertion of P3 prototype could compensate the release delay. Third, the surpass of the *stratum corneum* structure, which is the limiting step for transdermal absorption of molecules, tends to equalise the results obtained from different prototypes. Nonetheless, the most likely reason for these findings could be the limited experimental time in the FDC setup (0-8 h), which makes it difficult to detect actual differences. This timeframe was chosen in order to avoid an artificial permeability enhancement due to skin integrity loss, linked to the usual overhydration that can also affect the B_{12}@DMAPs [76].

In addition, B_{12} biodistribution at a 600-μm depth from P9 prototype is displayed in Fig. 4B. As a complementary study for a better understanding of the B_{12}@DMAPs dissolution process after insertion into the skin structure, *ex vivo* insertion studies were conducted. This experiment can be considered more accurate than the FDC permeability one, since the interstitial fluid is obviously more representative and the absence of skin overhydration allows the extension of the experiment in time. In general, the obtained results correlated better with the release studies, although certain timing differences can be observed, probably because of the above-mentioned differences in aqueous volumes between the *in vitro* release and *ex vivo* setups. A clear post-insertion time and polymer composition-dependent B_{12}@DMAPs disintegration and B_{12} skin deposition was observed (Fig. 4C). As expected, microneedles in prototype P9 disintegrated earlier and were almost completely dissolved after 4–8 h,

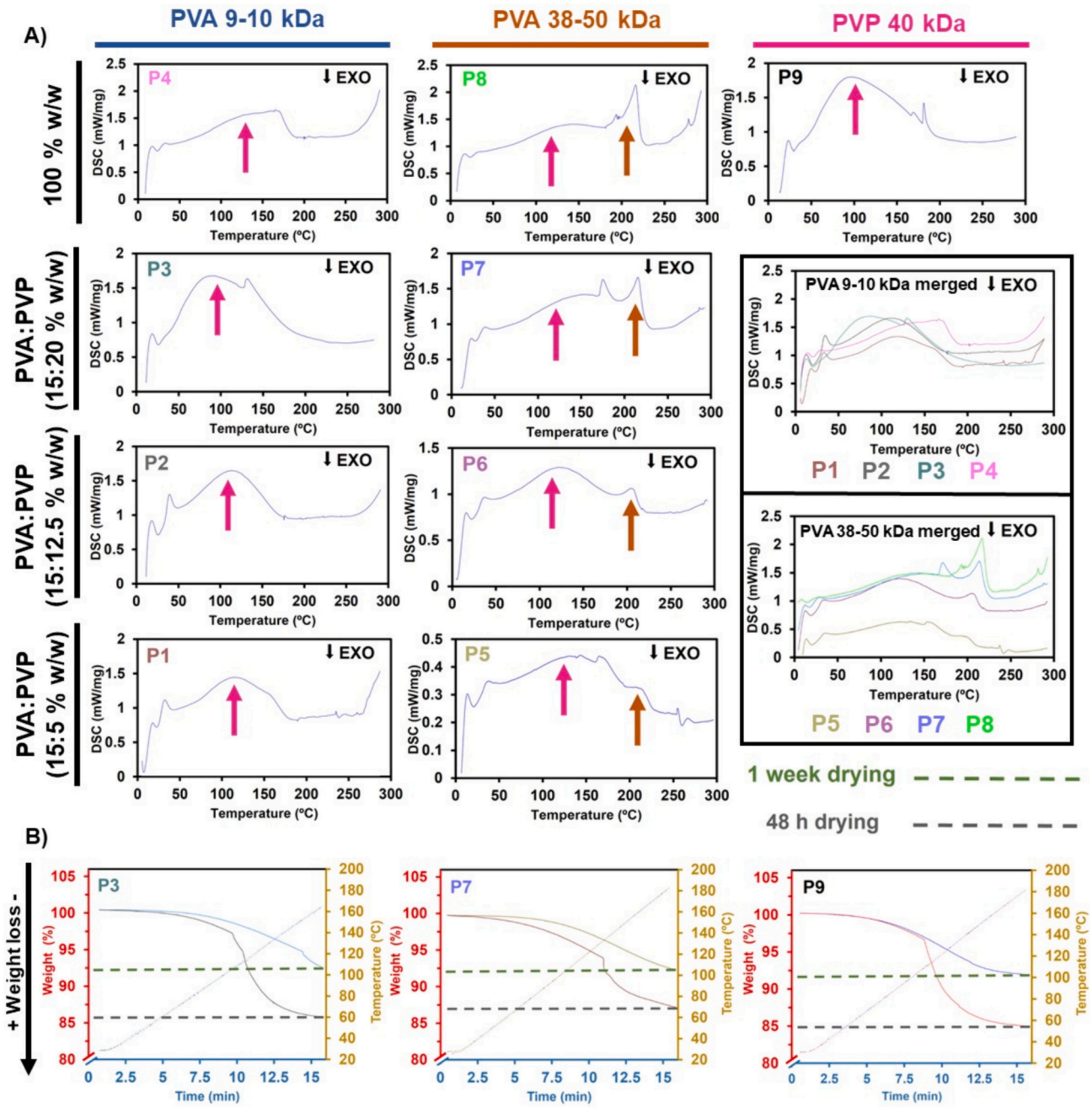

Fig. 3. a) DSC thermograms obtained from the analysis the different B_{12}@DMAPs. Pink arrows denote PVP characteristic signal in the 50–150 °C range. Orange arrows denote PVA (38–50 kDa) characteristic peak at 210–220 °C; **b)** TGA thermograms obtained from the analysis the different P3, P7 and P9 prototypes after demoulding (48 h) and 1-week drying: P3 after 48 h (black) and 1 week (blue), P7 after 48 h (red) and 1 week (green), P9 after 48 h (red) and 1 week (blue). (For interpretation of the references to colour in this figure legend, the reader is referred to the web version of this article.)

with an effective B_{12} skin deposition detected visually, whereas P3 needed around 12 h to achieve a major disintegration and increase drug deposition. This result strongly agrees with the outcome of the drug release kinetic modelling, since a 2.5-fold drug release rate increase was observed when comparing P9 and P3. Besides, P7 prototype did not show a complete dissolution of the polymer matrix as occurred in the dissolution tests and no B_{12} deposition was detected by naked eye in the inner side of the skin explant.

Finally, and before proceeding to the *in vivo* experimentation, B_{12}@DMAPs underwent biocompatibility studies to ensure their safety, although PVA and PVP are polymers commonly used in formulation, with a safe profile for most cell lines [77,78]. For this purpose, keratinocytes (HaCaT) and fibroblasts (L929) were chosen as representative skin cells [79,80]. Cell viability was determined by measuring ATP content in metabolically active cells using the CellTiter-Glo® assay after 24 h of exposure to different concentrations of polymeric B_{12}@DMAPs constituents, co-dissolved with the previously determined B_{12} dose loaded in the DMAPs needles (Fig. 4D-E). The 24 h exposure time was selected as it was the planned application time for B_{12}@DMAPs in subsequent *in vivo* studies. Cell viability after 24 h was >80 % which is considered the non-toxic threshold for biomedical devices development [81]. As expected, no toxic effects were detected even using the highest polymer concentrations, which much higher than the polymer amounts expected in a real situation, in the following *in vivo* studies or in a further clinical translation of the devices.

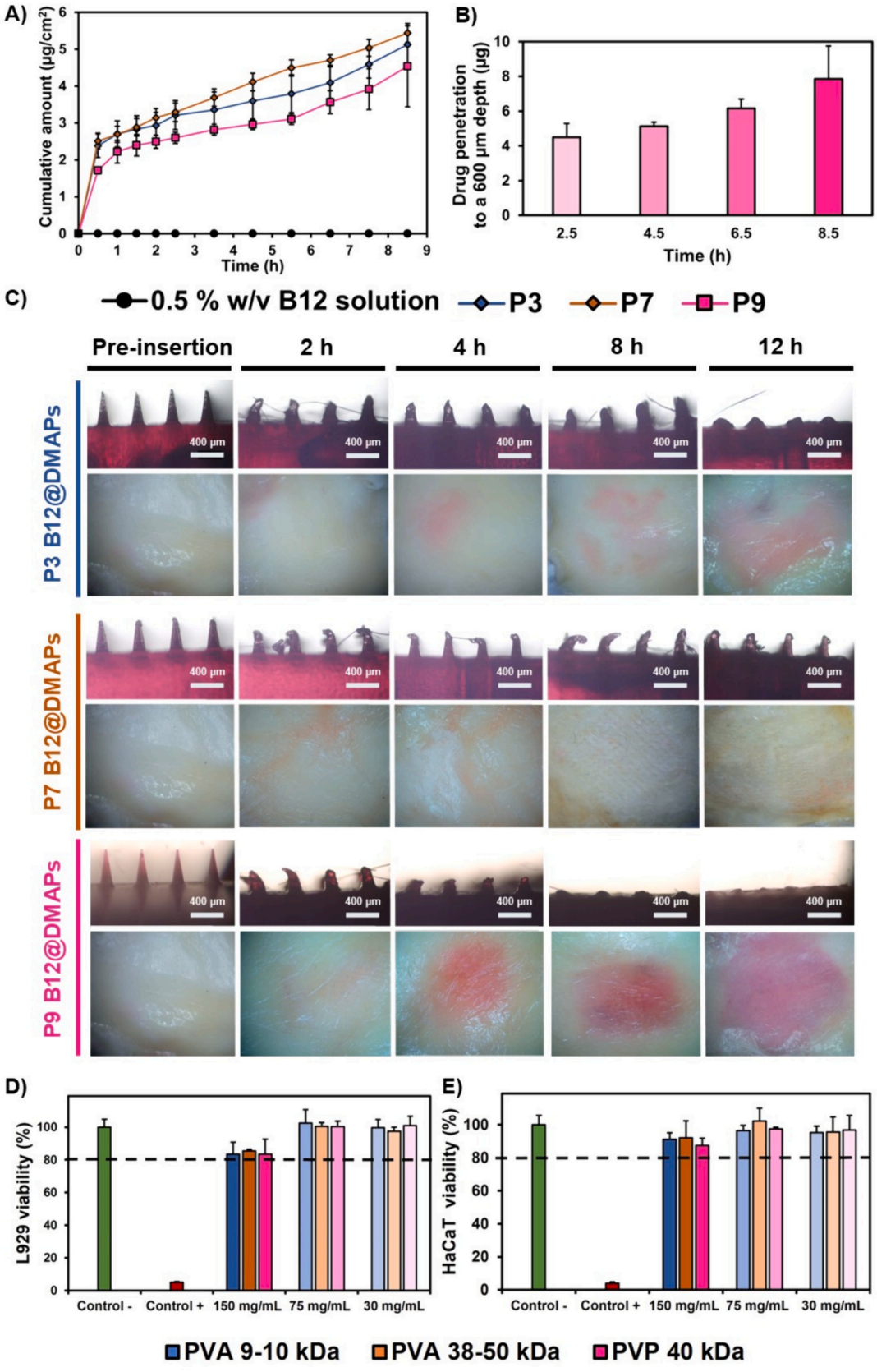

Fig. 4. a) *In vitro* permeability profiles of B_{12} delivered from different dissolving B_{12}@DMAP prototypes (P3, P7 and P9) through 600-µm dermatomed skin. All results are expressed as mean ± SD (n = 4); **b)** B_{12} biodistribution (µg) at a 600-µm depth from P9 prototype after 2.5, 4.5, 6.5 and 8.5 h post-insertion; **c)** Representative pictures pre- and post-insertion of B_{12}@DMAPs and B_{12} skin deposition (internal skin side) at 600-µm depth approximately. Scale bar: 400 µm; **d)** L929 fibroblast cell viability after 24 h of treatment with B_{12}@DMAP components. Results expressed as mean (percentage) ± SD. Discontinuous black line indicates 80 % cell viability; **e)** HaCaT keratinocyte cell viability after 24 h of treatment with B_{12}@DMAP components. Results expressed as mean (percentage) ± SD.

Table 4
Jmax and Kp of B_{12} delivered from the different B_{12}@DMAPs prototypes through 600-μm dermatomed skin ($n = 4$).

B_{12}@DMAPs prototype	J max (μg/cm^2/h)	Kp •10^{-6} (cm/s)
P3	0.20 ± 0.01	1.09 ± 0.08
P7	0.23 ± 0.02	1.28 ± 0.09
P9	0.23 ± 0.07	1.27 ± 0.37

3.4. Inflammation relapse in an in vivo delayed-type hypersensitivity model

In light of the findings reported from the characterisation, *in vitro* and *ex vivo* studies, P9 prototype was selected for the *in vivo* study to follow the 3 Rs principle for animal experimentation and reduce the number of animals used [82]. The main reason that supported this choice was that it provided a better B_{12} penetration enhancement compared to the other prototypes with a significant less dissolution time *ex vivo*. Therefore, the impact of potential B_{12}@DMAPs undesired removal during the 24 h-experiment *in vivo* would affect the B_{12} skin delivery less critically.

The effectiveness of the formulation was evaluated in a delayed-type hypersensitivity murine model, which has already been proposed as a mimicking model of inflammatory skin diseases where oxidative stress plays a key role [83]. First, the successful B_{12}@DMAPs insertion was assessed *in vivo* by observing the micro-channels created in histological sections (Fig. 5A). Histological sections showed holes around 200-μm depth, spaced at regular intervals. This penetration depth is shorter in

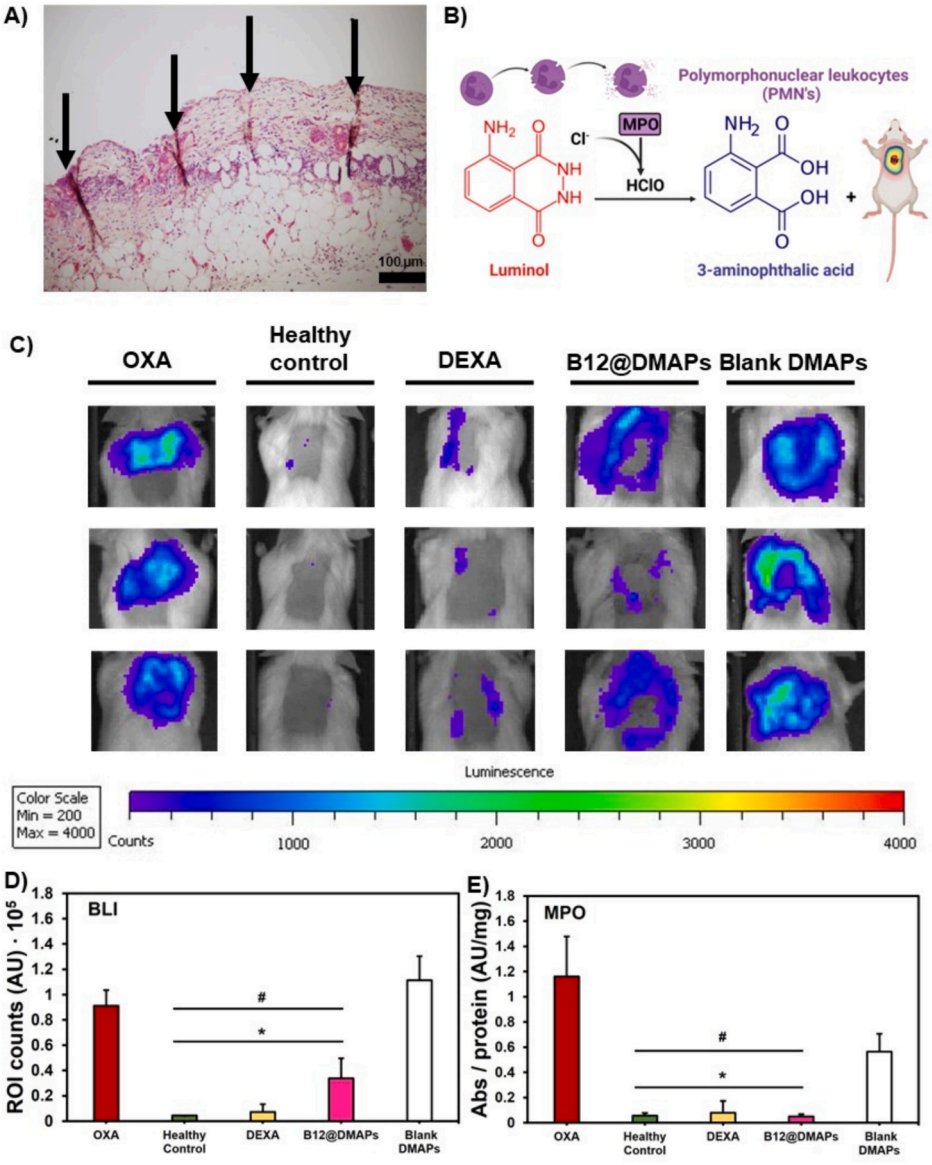

Fig. 5. **a)** Representative histology image of B_{12}@DMAPs insertion (H&E stain). Arrows indicate the specific insertion spots of B_{12}@DMAPs. Scale bar: 100 μm; **b)** Illustration of luminol-oxidation BLI mechanism *via* neutrophilic mediation; **c)** Representative images of BLI luminescence 24 h after OXA challenge of the different groups involved in the experiment: 1) non-treated group after OXA challenge -OXA- (negative control); 2) unchallenged healthy control group (naïve); 3) Group treated with dexamethasone after OXA challenge -DEXA- (positive control); 4) group treated with B_{12}@DMAPs [prototype P9] after OXA challenge -B_{12}@DMAPs-; 5) group treated with blank DMAPs [prototype P9] after OXA challenge -blank DMAPs-. Scale set from 200 (minimum) up to 4000 photons (maximum); **d)** BLI-induced ROI counts after the different treatments. Regions of interest (ROI) were precisely selected on the DMAPs insertion sites and set equal for each subject under study. Results are expressed as mean ± SD ($n = 6$); **e)** MPO activity quantification in skin tissue after the different treatments. MPO activity is expressed as absorbance/mg of protein. Results are expressed as mean ± SD ($n = 3$). * denotes statistically significant differences in comparison to OXA group ($p < 0.05$). # denotes statistically significant differences in comparison to blank DMAPs group ($p < 0.05$).

comparison to the preliminary depth obtained using the Parafilm® M model, probably due to the skin elasticity, which considerably reduces the penetration capacity of DMAPs [84]. However, this insertion depth ensures the complete bypass of the *stratum corneum*, which is 10–20 μm thick.

Bioluminescence imaging was used as an indirect MPO activity measurement, typically increased in inflammatory skin processes with white-cells infiltration (Fig. 5B). Briefly, MPO produces HClO, which oxidises luminol to 3-aminophthalic acid emitting a photon as a result of the chemical reaction [85]. MPO positive neutrophils are involved in the early phases of intense inflammation [86,87], thus BLI can be used for inflammation tracking. Untreated animals (OXA) and animals treated with Blank DMAPs showed the maximum levels of photon emission (Fig. 5C). Moreover, the absence of any photon emission in the DEXA group, which fulfils the role of positive control, demonstrates that the pathological process can be completely retrieved in terms of bioluminescence emission, due to the absence of BLI signal from the back areas where DEXA was topically applied. Mice treated with B_{12}@DMAPs could also effectively normalise the bioluminescence emission on the skin area in which the devices were administered; however, a lack of radiant effect was observed, since the areas surrounding the point of DMAP insertion still showed an important bioluminescence signal. This behaviour was also observed in previous studies carried out with polymeric DMAPs in this same model [34]. Nevertheless, the central area where BLI signal was similar to DEXA and naïve (healthy control) groups is a clear sign of inflammatory amelioration. The success of the different treatments was concurrently quantified by ROI counts determination (Fig. 5D), and direct determination of MPO activity in skin biopsies taken from the specific B_{12}@DMAPs insertion area (Fig. 5E). Again, B_{12}@DMAPs showed significant differences in both parameters in comparison to OXA and Blank DMAPs groups ($p < 0.05$), pointing out that B_{12}@DMAPs effectively reduced the inflammatory reaction. This finding was specially marked for MPO determination, where no statistical differences were observed for B_{12}@DMAPs when compared to DEXA and healthy control groups ($p > 0.05$). Hence, these findings suggest once again that B_{12}@DMAPs treatment could reduce the pro-inflammatory response of neutrophils under oxidative stress environment.

Histopathological analysis was performed to assess the protection capacity of the formulation against anatomical damage and physiopathological changes induced by the inflammatory processes. From histological sections with H&E stain (Fig. 6A), it could be observed that following B_{12}@DMAPs administration, animals showed minimum inflammatory-associated damage. Particularly, no spongiotic patterns were observed and the leukocyte infiltration was comparable with the one observed in animals treated with DEXA as well as in the healthy group. In contrast, the OXA group showed high rates of leukocyte presence in the tissue and even spongiotic patterns, indicating a great damage in the skin structure after 24 h. Dermatitis and psoriasis-related pathologies are also characterised by an anomalous dermal swelling and epidermal acanthosis (hyperplasia) [88], which was observed in untreated animals (OXA) and normalised after DEXA treatment ($p < 0.05$) (Fig. 6A-C). Besides, a thinner epidermal structure was detected in DEXA group when compared to healthy animals (Fig. 6B), probably because of the skin atrophy that corticosteroids can induce from the beginning of the treatments [89]. In the same way, animals treated with blank DMAPs showed the highest epidermal growth, suggesting that DMAP application could induce a discrete skin damage [34]. However, after B_{12}@DMAPs treatment, epidermal thickness decreased significantly compared to blank DMAPs ($p < 0.05$), and no differences were found when compared either with healthy animals or DEXA group ($p > 0.05$) (Fig. 6B). Fibrotic deposition is another sign related to dermal growth in dermatitis and psoriasis pathologies, however it is a delayed event that usually appears 72 h after inflammation challenge [90]. This is why no marked differences were observed when comparing collagen deposition between the OXA and B_{12}@DMAP groups (Fig. 6C). Nevertheless, B_{12}@DMAPs could effectively reverse collagen deposition associated with microneedle insertion (blank DMAPs group), similarly to what was observed in BLI and epidermis thickness studies.

It is well-known that oxidative stress in inflammatory skin models triggers gene overexpression of several pro-inflammatory cytokines, such as IL-1β, IL-4, IL-6 and TNF-α, contributing to the dermatitis and psoriasis pathogenesis [85]. On one hand, IL-1β and IL- 4 play a notable role in atopic dermatitis and the over-expression of these cytokines is related with the promotion of inflammatory skin lesions [91,92]. On the other hand, IL-6 and TNF-α induce vascular endothelial growth factor-A that also correlates with inflammation severity [93]. For all the pro-inflammatory cytokines studied here, the same trend was observed: levels were similarly overexpressed in the OXA group and in animals treated with blank DMAPs, being specially marked for IL-6, which is particularly involved in the acute inflammation phase (Figs. 6D-G). These cytokines levels (IL-1β, IL-4 and TNF-α) were normalised after the administration of B_{12}@DMAPs treatment, being similar to those ones found in healthy control and DEXA ($p > 0.05$), and significantly different in comparison to OXA and blank DMAPs ($p < 0.05$). In the case of IL-6, although no statistical differences were detected between B_{12}@DMAPs, DEXA and healthy groups ($p > 0.05$), a less marked downregulation was observed, probably because of the above-mentioned role of IL-6 in the acute phase of the inflammatory process, which causes a higher interleukin secretion. Overall, the results obtained agree that B_{12}@DMAPs can effectively relapse inflammation *in vivo*, reduce the recruitment response of neutrophils and anatomic damage, and inhibit the secretion of pro-inflammatory mediators.

4. Conclusion

In summary, B_{12}@DMAPs were shown to be optimal devices to facilitate B_{12} delivery to deep skin layers in an *ex vivo* FDC setup, as passive diffusion is negligible when B_{12} is administered in free form due to its large molecular weight. PVP and PVA combinations led to devices with improved mechanical properties, namely high resistance to compression and high insertion capacity. However, B_{12} release was slower than the one observed with PVP-only DMAPs. *In vitro* experiments in fibroblasts and keratinocytes pointed out the biocompatibility of B_{12}@DMAPs with characteristic skin cell lines. An *in vivo* inflammatory skin reaction model was used to test B_{12}@DMAPs efficacy. The treatment decreased bioluminescence signals, myeloperoxidase activity and pro-inflammatory cytokine levels at the insertion site, with results comparable to those achieved by a topical corticosteroid treatment which has well-known side-effects usually. Furthermore, histological observations denoted a normalisation of anatomical damage following B_{12}@DMAPs treatments. Altogether, the obtained results suggests that B_{12}@DMAPs are an alternative to current therapies for inflammatory skin conditions, such as dermatitis and psoriasis. In particular, this approach can overcome the considerable side effects caused by conventional therapies, particularly when used in a long-term chronic treatment.

Funding

This publication is part of the grant PID2020-114530GA-I00 funded by MCIN/AEI/10.13039/501100011033. A.J.G. acknowledges the financial support from “Atracció de Talent” grant (ref: UV-INV-PREDOC-18F2–743816) funded by the University of Valencia, and “Margarita Salas” grant (ref: MS21–126) funded by the Spanish Ministry of Universities and European Union (Next generation-EU). M.M-N. acknowledges the financial support from ACIF grant funded by Generalitat Valenciana; Conselleria d’Innovació, Universitats, Ciència i Societat Digital (ref: CIACIF/2022/341). H.A.S. acknowledges the UMCG Research Funds for financial support.

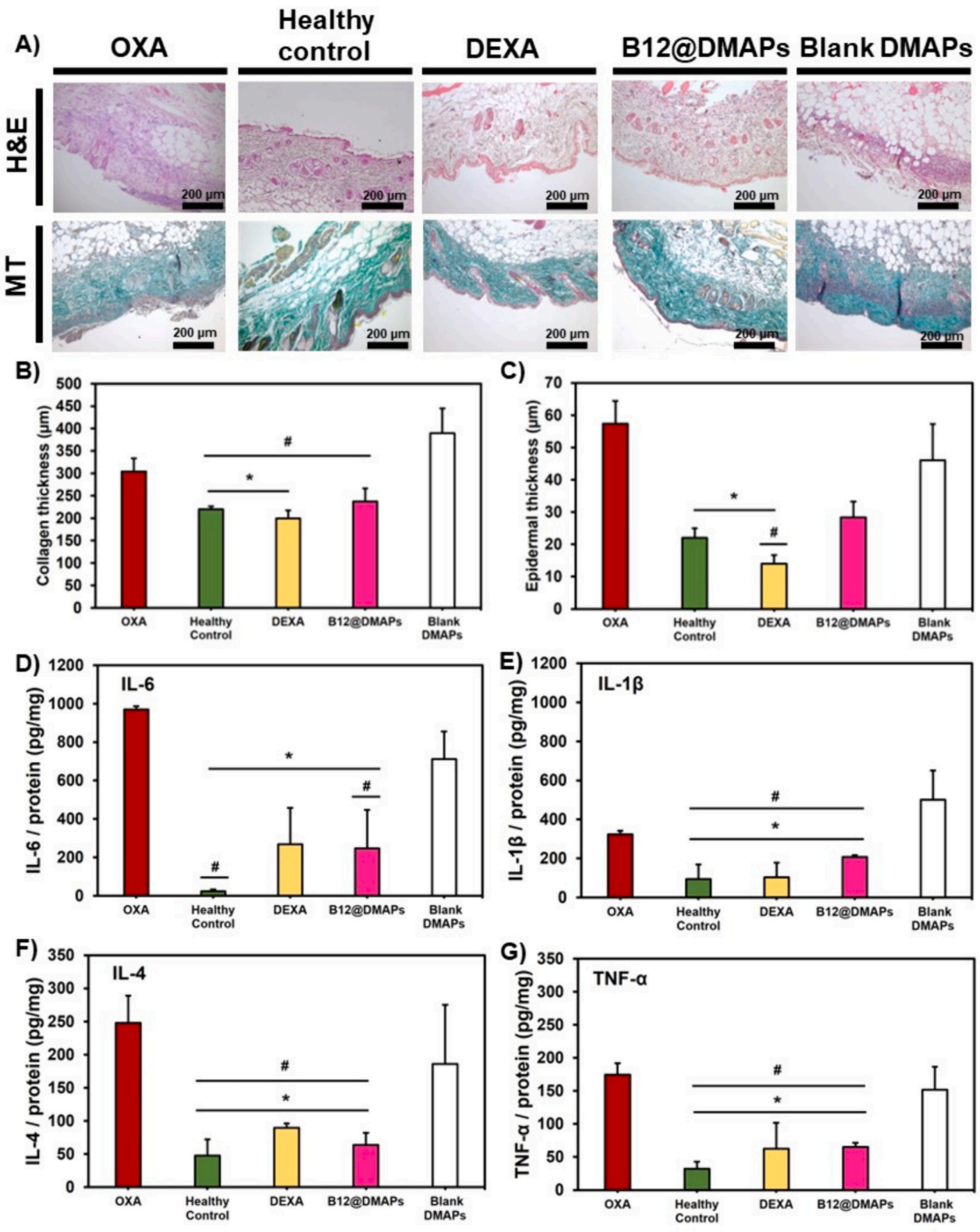

Fig. 6. **a)** Representative images from the histological sections stained with H&E and MT stains (20× magnifications). Scale bar: 200 μm; **b)** Epidermal thickness measured from histological observation (H&E stain) 24 h after the administration of the different treatments (10× magnification); **c)** Collagen thickness measured from histological observation (MT stain) 24 h after the administration of the different treatments (10× magnification); **d)** IL-6 quantification detected by ELISA immunoassay in skin biopsies; **e)** IL-1β quantification detected by ELISA immunoassay in skin biopsies; **f)** IL-4 quantification detected by ELISA immunoassay in skin biopsies; **g)** TNF-α quantification detected by ELISA immunoassay in skin biopsies. Cytokine levels are expressed as absorbance/mg of protein. Results are expressed as mean ± SD ($n = 3$). * denotes statistically significant differences in comparison to OXA group ($p < 0.05$). # denotes statistically significant differences in comparison to blank DMAPs group ($p < 0.05$).

Ethics approval

This study was performed in line with the principles of the Declaration of Helsinki. Approval was granted by the Ethics Committee of University Valencia (2023-VSC-PEA-0064).

CRediT authorship contribution statement

Antonio José Guillot: Writing – original draft, Visualization, Validation, Supervision, Software, Resources, Methodology, Investigation, Formal analysis, Data curation, Conceptualization. **Miquel Martínez-Navarrete:** Writing – review & editing, Investigation, Formal analysis, Data curation. **Rosa Maria Giner:** Writing – review & editing, Visualization, Investigation. **Maria Carmen Recio:** Writing – review & editing, Visualization, Investigation. **Helder A. Santos:** Writing – review & editing, Resources, Funding acquisition. **Ana Sara Cordeiro:** Writing – review & editing, Visualization, Supervision, Resources, Methodology, Investigation, Funding acquisition, Formal analysis. **Ana Melero:** Writing – review & editing, Visualization, Supervision, Resources, Methodology, Investigation, Funding acquisition, Formal analysis, Conceptualization.

Declaration of competing interest

The authors have no relevant financial or non-financial interests to disclose.

Data availability

The data that support the findings of this study are available from the corresponding author upon reasonable request.

Acknowledgements

Authors acknowledge assistance provided by Inmaculada Noguera Salvá and Eva Blanch Torres for successfully carrying out the *in vivo*. Graphical abstract, Fig. 1 and 6A were created using Biorender under an active licence.

Appendix A. Supplementary data

Supplementary data to this article can be found online at https://doi.org/10.1016/j.jconrel.2024.09.032.

References

[1] C.A. Juan, J.M. Pérez de la Lastra, F.J. Plou, E. Pérez-Lebeña, The chemistry of reactive oxygen species (ROS) revisited: outlining their role in biological macromolecules (DNA, lipids and proteins) and induced pathologies, Int. J. Mol. Sci. 22 (2021) 4642, https://doi.org/10.3390/ijms22094642.
[2] W. Yu, Y. Tu, Z. Long, J. Liu, D. Kong, J. Peng, H. Wu, G. Zheng, J. Zhao, Y. Chen, R. Liu, W. Li, C. Hai, Reactive oxygen species bridge the gap between chronic inflammation and tumor development, Oxid. Med. Cell. Longev. 2022 (2022) 2606928, https://doi.org/10.1155/2022/2606928.
[3] S. Reuter, S.C. Gupta, M.M. Chaturvedi, B.B. Aggarwal, Oxidative stress, inflammation, and cancer: how are they linked? Free Radic. Biol. Med. 49 (2010) 1603–1616, https://doi.org/10.1016/j.freeradbiomed.2010.09.006.
[4] Y.S. Ryu, K.A. Kang, M.J. Piao, M.J. Ahn, J.M. Yi, Y.-M. Hyun, S.H. Kim, M.K. Ko, C.O. Park, J.W. Hyun, Particulate matter induces inflammatory cytokine production via activation of NFκB by TLR5-NOX4-ROS signaling in human skin keratinocyte and mouse skin, Redox Biol. 21 (2019) 101080, https://doi.org/10.1016/j.redox.2018.101080.
[5] F.J. Martínez-Navarro, F.J. Martínez-Morcillo, A. López-Muñoz, I. Pardo-Sánchez, T. Martínez-Menchón, R. Corbalán-Vélez, M.L. Cayuela, A.B. Pérez-Oliva, D. García-Moreno, V. Mulero, The vitamin B6-regulated enzymes PYGL and G6PD fuel NADPH oxidases to promote skin inflammation, Dev. Comp. Immunol. 108 (2020) 103666, https://doi.org/10.1016/j.dci.2020.103666.
[6] J.N. Sharma, A. Al-Omran, S.S. Parvathy, Role of nitric oxide in inflammatory diseases, Inflammopharmacology 15 (2007) 252–259, https://doi.org/10.1007/s10787-007-0013-x.
[7] E.L. Theiss, L.V. Griebsch, A.A. Lauer, D. Janitschke, V.K.J. Erhardt, E.C. Haas, K. N. Kuppler, J. Radermacher, O. Walzer, D. Portius, H.S. Grimm, T. Hartmann, M.O. W. Grimm, Vitamin B12 attenuates changes in phospholipid levels related to oxidative stress in SH-SY5Y cells, Cells 11 (2022) 2574, https://doi.org/10.3390/cells11162574.
[8] Y.-M. Jeon, Y. Kwon, S. Lee, S. Kim, M. Jo, S. Lee, S.R. Kim, K. Kim, H.-J. Kim, Vitamin B12 reduces TDP-43 toxicity by alleviating oxidative stress and mitochondrial dysfunction, Antioxid, Basel Switz. 11 (2021) 82, https://doi.org/10.3390/antiox11010082.
[9] A.K. Offringa, A.R. Bourgonje, M.S. Schrier, R.C. Deth, H. van Goor, Clinical implications of vitamin B12 as redox-active cofactor, Trends Mol. Med. 27 (2021) 931–934, https://doi.org/10.1016/j.molmed.2021.07.002.
[10] U.K. Misra, J. Kalita, S.K. Singh, S.K. Rahi, Oxidative stress markers in vitamin B12 deficiency, Mol. Neurobiol. 54 (2017) 1278–1284, https://doi.org/10.1007/s12035-016-9736-2.
[11] E.E. van de Lagemaat, L.C.P.G.M. de Groot, E.G.H.M. van den Heuvel, Vitamin B12 in relation to oxidative stress: a systematic review, Nutrients 11 (2019) 482, https://doi.org/10.3390/nu11020482.
[12] A.J. Guillot, M. Martínez-Navarrete, T.M. Garrigues, A. Melero, Skin drug delivery using lipid vesicles: a starting guideline for their development, J. Control. Release 355 (2023) 624–654, https://doi.org/10.1016/j.jconrel.2023.02.006.
[13] J.D. Bos, M.M. Meinardi, The 500 Dalton rule for the skin penetration of chemical compounds and drugs, Exp. Dermatol. 9 (2000) 165–169, https://doi.org/10.1034/j.1600-0625.2000.009003165.x.
[14] A.J. Guillot, E. Jornet-Mollá, N. Landsberg, C. Milián-Guimerá, M.C. Montesinos, T. M. Garrigues, A. Melero, Cyanocobalamin Ultraflexible lipid vesicles: characterization and in vitro evaluation of drug-skin depth profiles, Pharmaceutics 13 (2021) 418, https://doi.org/10.3390/pharmaceutics13030418.
[15] R. Gupta, B.S. Dwadasi, B. Rai, S. Mitragotri, Effect of chemical permeation enhancers on skin permeability: in silico screening using molecular dynamics simulations, Sci. Rep. 9 (2019) 1456, https://doi.org/10.1038/s41598-018-37900-0.
[16] J. Ruan, C. Liu, J. Wang, T. Zhong, P. Quan, L. Fang, Efficacy and safety of permeation enhancers: a kinetic evaluation approach and molecular mechanism study in the skin, Int. J. Pharm. 626 (2022) 122155, https://doi.org/10.1016/j.ijpharm.2022.122155.
[17] T.H. Baryakova, B.H. Pogostin, R. Langer, K.J. McHugh, Overcoming barriers to patient adherence: the case for developing innovative drug delivery systems, Nat. Rev. Drug Discov. 22 (2023) 387–409, https://doi.org/10.1038/s41573-023-00670-0.
[18] M. Roustit, S. Blaise, J.-L. Cracowski, Trials and tribulations of skin iontophoresis in therapeutics, Br. J. Clin. Pharmacol. 77 (2014) 63–71, https://doi.org/10.1111/bcp.12128.
[19] A.J. Guillot, M. Martínez-Navarrete, V. Zinchuk-Mironova, A. Melero, Microneedle-assisted transdermal delivery of nanoparticles: recent insights and prospects, Wiley Interdiscip. Rev. Nanomed. Nanobiotechnol. 15 (2023) e1884, https://doi.org/10.1002/wnan.1884.
[20] A.J. Guillot, A.S. Cordeiro, R.F. Donnelly, M.C. Montesinos, T.M. Garrigues, A. Melero, Microneedle-based delivery: an overview of current applications and trends, Pharmaceutics 12 (2020) 569, https://doi.org/10.3390/pharmaceutics12060569.
[21] T. Bauleth-Ramos, N. El-Sayed, F. Fontana, M. Lobita, M.-A. Shahbazi, H.A. Santos, Recent approaches for enhancing the performance of dissolving microneedles in drug delivery applications, Mater. Today 63 (2023) 239–287, https://doi.org/10.1016/j.mattod.2022.12.007.
[22] I.K. Ramöller, I.A. Tekko, H.O. McCarthy, R.F. Donnelly, Rapidly dissolving bilayer microneedle arrays - a minimally invasive transdermal drug delivery system for vitamin B12, Int. J. Pharm. 566 (2019) 299–306, https://doi.org/10.1016/j.ijpharm.2019.05.066.
[23] E. Del Duca, F. Farnetani, N. De Carvalho, U. Bottoni, G. Pellacani, S.P. Nisticò, Superiority of a vitamin B12-containing emollient compared to a standard emollient in the maintenance treatment of mild-to-moderate plaque psoriasis, Int. J. Immunopathol. Pharmacol. 30 (2017) 439–444, https://doi.org/10.1177/0394632017736674.
[24] M. Stücker, U. Memmel, M. Hoffmann, J. Hartung, P. Altmeyer, Vitamin B(12) cream containing avocado oil in the therapy of plaque psoriasis, Dermatol, Basel Switz. 203 (2001) 141–147, https://doi.org/10.1159/000051729.
[25] R. Januchowski, Evaluation of topical vitamin B(12) for the treatment of childhood eczema, J. Altern. Complement. Med. 15 (2009) 387–389, https://doi.org/10.1089/acm.2008.0497.
[26] S. Barbarot, S. Auziere, A. Gadkari, G. Girolomoni, L. Puig, E.L. Simpson, D. J. Margolis, M. de Bruin-Weller, L. Eckert, Epidemiology of atopic dermatitis in adults: results from an international survey, Allergy 73 (2018) 1284–1293, https://doi.org/10.1111/all.13401.
[27] M.V. Angles, C.A. Antonietti, A.C. Torre, E. Juszkiewicz Franzé, L.D. Mazzuoccolo, C.A.S. Parisi, Prevalence of atopic dermatitis in adults, An. Bras. Dermatol. 97 (2022) 107–109, https://doi.org/10.1016/j.abd.2020.10.016.
[28] G. Damiani, N.L. Bragazzi, C. Karimkhani Aksut, D. Wu, G. Alicandro, D. McGonagle, C. Guo, R. Dellavalle, A. Grada, P. Wong, C. La Vecchia, L.-S. Tam, K. D. Cooper, M. Naghavi, The Global, Regional, and National Burden of Psoriasis: Results and Insights From the Global Burden of Disease 2019 Study, Front. Med. 8 (2021) 743180. doi:https://doi.org/10.3389/fmed.2021.743180.
[29] C.-C. Lee, Y.-J. Peng, C.-C. Lu, H.-C. Chen, F.-C. Yeh, Corticosteroid-induced liver injury in adult-onset Still's disease, Med. Kaunas Lith. 58 (2022) 191, https://doi.org/10.3390/medicina58020191.
[30] M. Lam, J.W. Zhu, M. Tadrous, A.M. Drucker, Association between topical Calcineurin inhibitor use and risk of Cancer, Including Lymphoma, Keratinocyte Carcinoma, and Melanoma: A Systematic Review and Meta-analysis, JAMA

Dermatol 157 (2021) 549–558, https://doi.org/10.1001/jamadermatol.2021.0345.
[31] F. Besemer, C. Kramers, K. Brinkman, A.R.M.M. Hermus, A.E. van Herwaarden, D. M. Burger, Hypothalamic–pituitary–adrenal axis suppression by inhaled or nasal corticosteroids in HIV-infected patients, Int. J. Clin. Pharmacol. 42 (2020) 347–350, https://doi.org/10.1007/s11096-020-00995-5.
[32] M. Oray, K. Abu Samra, N. Ebrahimiadib, H. Meese, C.S. Foster, Long-term side effects of glucocorticoids, expert Opin, Drug Saf. 15 (2016) 457–465, https://doi.org/10.1517/14740338.2016.1140743.
[33] ICH Q2(R2) Validation of analytical procedures - Scientific guideline | European Medicines Agency, in: https://www.ema.europa.eu/en/ich-q2r2-validation-analytical-procedures-scientific-guideline, 2024 (accessed May 15, 2024).
[34] M. Martínez-Navarrete, A.J. Guillot, M.C. Lobita, M.C. Recio, R. Giner, J. Aparicio-Blanco, M.C. Montesinos, H.A. Santos, A. Melero, Cyclosporin A-loaded dissolving microneedles for dermatitis therapy: development, characterisation and efficacy in a delayed-type hypersensitivity in vivo model, Drug Deliv. Transl. Res. (2024), https://doi.org/10.1007/s13346-024-01542-9.
[35] A.D. Permana, I.A. Tekko, M.T.C. McCrudden, Q.K. Anjani, D. Ramadon, H. O. McCarthy, R.F. Donnelly, Solid lipid nanoparticle-based dissolving microneedles: a promising intradermal lymph targeting drug delivery system with potential for enhanced treatment of lymphatic filariasis, J. Control. Release 316 (2019) 34–52, https://doi.org/10.1016/j.jconrel.2019.10.004.
[36] M.C. Lobita, N. El-Sayed, J.F. Pinto, H.A. Santos, Development of fast dissolving polymer-based microneedles for delivery of an antigenic melanoma cell membrane, Int. J. Pharm. 642 (2023) 123143, https://doi.org/10.1016/j.ijpharm.2023.123143.
[37] J.-F. Liao, J.-C. Lee, C.-K. Lin, K.-C. Wei, P.-Y. Chen, H.-W. Yang, Self-assembly DNA Polyplex vaccine inside dissolving microneedles for high-potency intradermal vaccination, Theranostics 7 (2017) 2593–2605, https://doi.org/10.7150/thno.19894.
[38] R.F. Donnelly, R. Majithiya, T.R.R. Singh, D.I.J. Morrow, M.J. Garland, Y.K. Demir, K. Migalska, E. Ryan, D. Gillen, C.J. Scott, A.D. Woolfson, Design, optimization and characterisation of polymeric microneedle arrays prepared by a novel laser-based micromoulding technique, Pharm. Res. 28 (2011) 41–57, https://doi.org/10.1007/s11095-010-0169-8.
[39] E. Larrañeta, J. Moore, E.M. Vicente-Pérez, P. González-Vázquez, R. Lutton, A. D. Woolfson, R.F. Donnelly, A proposed model membrane and test method for microneedle insertion studies, Int. J. Pharm. 472 (2014) 65–73, https://doi.org/10.1016/j.ijpharm.2014.05.042.
[40] E. Larrañeta, S. Stewart, S.J. Fallows, L.L. Birkhäuer, M.T.C. McCrudden, A. D. Woolfson, R.F. Donnelly, A facile system to evaluate in vitro drug release from dissolving microneedle arrays, Int. J. Pharm. 497 (2016) 62–69, https://doi.org/10.1016/j.ijpharm.2015.11.038.
[41] C. D'Amico, F. Fontana, N. El-Sayed, K. Elbadri, A. Correia, A. Rahikkala, J. Saarinen, M.-A. Shahbazi, H.A. Santos, Double-layered Polyvinylpyrrolidone–poly(methyl vinyl ether-alt-maleic acid)-based microneedles to deliver meloxicam: an in vitro, in vivo, and short-term stability evaluation study, Adv. Ther. 6 (2023) 2300138, https://doi.org/10.1002/adtp.202300138.
[42] P.L. Ritger, N.A. Peppas, A simple equation for description of solute release I. Fickian and non-fickian release from non-swellable devices in the form of slabs, spheres, cylinders or discs, J. Control. Release 5 (1987) 23–36, https://doi.org/10.1016/0168-3659(87)90034-4.
[43] P.L. Ritger, N.A. Peppas, A simple equation for description of solute release II. Fickian and anomalous release from swellable devices, J. Control. Release 5 (1987) 37–42, https://doi.org/10.1016/0168-3659(87)90035-6.
[44] R.W. Korsmeyer, R. Gurny, E. Doelker, P. Buri, N.A. Peppas, Mechanisms of solute release from porous hydrophilic polymers, Int. J. Pharm. 15 (1983) 25–35, https://doi.org/10.1016/0378-5173(83)90064-9.
[45] H. Kim, R. Fassihi, Application of binary polymer system in drug release rate modulation. 2. Influence of formulation variables and hydrodynamic conditions on release kinetics, J. Pharm. Sci. 86 (1997) 323–328, https://doi.org/10.1021/js960307p.
[46] N.A. Peppas, J.J. Sahlin, A simple equation for the description of solute release. III. Coupling of diffusion and relaxation, Int. J. Pharm. 57 (1989) 169–172, https://doi.org/10.1016/0378-5173(89)90306-2.
[47] D. Ramadon, F. Ulayya, A.S. Qur'ani, I. Iskandarsyah, Y. Harahap, Q.K. Anjani, V. Aileen, P. Hartrianti, R.F. Donnelly, Combination of dissolving microneedles with Nanosuspension and co-grinding for transdermal delivery of Ketoprofen, Pharm. Basel Switz. 16 (2023) 378, https://doi.org/10.3390/ph16030378.
[48] C. Kolluru, Y. Gomaa, M.R. Prausnitz, Development of a thermostable microneedle patch for polio vaccination, drug Deliv, Transl. Res. 9 (2019) 192–203, https://doi.org/10.1007/s13346-018-00608-9.
[49] A.D. Permana, M.T.C. McCrudden, R.F. Donnelly, Enhanced intradermal delivery of Nanosuspensions of Antifilariasis drugs using dissolving microneedles: a proof of concept study, Pharmaceutics 11 (2019) 346, https://doi.org/10.3390/pharmaceutics11070346.
[50] A.J. Guillot, P. Merino-Gutiérrez, A. Bocchino, C. O'Mahony, R.M. Giner, M. C. Recio, T.M. Garrigues, A. Melero, Exploration of microneedle-assisted skin delivery of cyanocobalamin formulated in ultraflexible lipid vesicles, Eur. J. Pharm. Biopharm. 177 (2022) 184–198, https://doi.org/10.1016/j.ejpb.2022.06.015.
[51] K. Kehe, M. Abend, K. Kehe, R. Ridi, R.U. Peter, D. van Beuningen, Tissue engineering with HaCaT cells and a fibroblast cell line, Arch. Dermatol. Res. 291 (1999) 600–605, https://doi.org/10.1007/s004030050461.
[52] A. Idrees, V. Chiono, G. Ciardelli, S. Shah, R. Viebahn, X. Zhang, J. Salber, Validation of in vitro assays in three-dimensional human dermal constructs, Int. J. Artif. Organs 41 (2018) 779–788, https://doi.org/10.1177/0391398818775519.
[53] M.C.J. Hofmann, M. Schmidt, O. Arne, G. Geisslinger, M.J. Parnham, N.M.W.J. de Bruin, Non-invasive bioluminescence imaging as a standardized assessment measure in mouse models of dermal inflammation, J. Dermatol. Sci. 91 (2018) 153–163, https://doi.org/10.1016/j.jdermsci.2018.04.013.
[54] Y.S. Heo, H.J. Song, Characterizing cutaneous elastic fibers by eosin fluorescence detected by fluorescence microscopy, Ann. Dermatol. 23 (2011) 44–52, https://doi.org/10.5021/ad.2011.23.1.44.
[55] H. Mao, P. Su, W. Qiu, L. Huang, H. Yu, Y. Wang, The use of Masson's trichrome staining, second harmonic imaging and two-photon excited fluorescence of collagen in distinguishing intestinal tuberculosis from Crohn's disease, Colorectal Dis. 18 (2016) 1172–1178, https://doi.org/10.1111/codi.13400.
[56] C.A. Schneider, W.S. Rasband, K.W. Eliceiri, NIH image to ImageJ: 25 years of image analysis, Nat. Methods 9 (2012) 671–675, https://doi.org/10.1038/nmeth.2089.
[57] J. Arasa, P. Martos, M.C. Terencio, F. Valcuende-Cavero, M.C. Montesinos, Topical application of the adenosine A2A receptor agonist CGS-21680 prevents phorbol-induced epidermal hyperplasia and inflammation in mice, Exp. Dermatol. 23 (2014) 555–560, https://doi.org/10.1111/exd.12461.
[58] S. Demartis, G. Rassu, V. Mazzarello, E. Larrañeta, A. Hutton, R.F. Donnelly, A. Dalpiaz, M. Roldo, A.J. Guillot, A. Melero, P. Giunchedi, E. Gavini, Delivering hydrosoluble compounds through the skin: what are the chances? Int. J. Pharm. 646 (2023) 123457 https://doi.org/10.1016/j.ijpharm.2023.123457.
[59] A. Ma'ali, H. Naseef, M. Qurt, A.D. Abukhalil, A.K. Rabba, I. Sabri, The preparation and evaluation of cyanocobalamin Mucoadhesive sublingual tablets, Pharm. Basel Switz. 16 (2023) 1412. doi:https://doi.org/10.3390/ph16101412.
[60] H. Lee, H.S. Min, M. Jang, G. Kang, S. Gong, C. Lee, Y.W. Song, U.-W. Jung, S. Lee, H.Y. Ryu, H. Yang, H. Jung, Lidocaine-loaded dissolving microneedle for safe local anesthesia on oral mucosa for dental procedure, Expert Opin. Drug Deliv. 20 (2023) 851–861, https://doi.org/10.1080/17425247.2023.2216450.
[61] M. Martínez-Navarrete, A. Pérez-López, A.J. Guillot, A.S. Cordeiro, A. Melero, J. Aparicio-Blanco, Latest advances in glucose-responsive microneedle-based systems for transdermal insulin delivery, Int. J. Biol. Macromol. 263 (2024) 130301, https://doi.org/10.1016/j.ijbiomac.2024.130301.
[62] E. Gonzalez-Gonzalez, T.J. Speaker, R.P. Hickerson, R. Spitler, M.A. Flores, D. Leake, C.H. Contag, R.L. Kaspar, Silencing of reporter gene expression in skin using siRNAs and expression of plasmid DNA delivered by a soluble protrusion Array device (PAD), Mol. Ther. 18 (2010) 1667–1674, https://doi.org/10.1038/mt.2010.126.
[63] M. Teodorescu, M. Bercea, S. Morariu, Biomaterials of PVA and PVP in medical and pharmaceutical applications: perspectives and challenges, Biotechnol. Adv. 37 (2019) 109–131, https://doi.org/10.1016/j.biotechadv.2018.11.008.
[64] R.F. Donnelly, M.J. Garland, D.I.J. Morrow, K. Migalska, T.R.R. Singh, R. Majithiya, A.D. Woolfson, Optical coherence tomography is a valuable tool in the study of the effects of microneedle geometry on skin penetration characteristics and in-skin dissolution, J. Control. Release 147 (2010) 333–341, https://doi.org/10.1016/j.jconrel.2010.08.008.
[65] S. Lau, J. Fei, H. Liu, W. Chen, R. Liu, Multilayered pyramidal dissolving microneedle patches with flexible pedestals for improving effective drug delivery, J. Control. Release 265 (2017) 113–119, https://doi.org/10.1016/j.jconrel.2016.08.031.
[66] M. Teodorescu, M. Bercea, S. Morariu, Miscibility study on polymer mixtures in dilute solution, Colloids Surf. A Physicochem. Eng. Asp. 559 (2018) 325–333, https://doi.org/10.1016/j.colsurfa.2018.09.062.
[67] Q.K. Anjani, A.D.C. Nainggolan, H. Li, A. Miatmoko, E. Larrañeta, R.F. Donnelly, Parafilm® M and Strat-M® as skin simulants in in vitro permeation of dissolving microarray patches loaded with proteins, Int. J. Pharm. 655 (2024) 124071, https://doi.org/10.1016/j.ijpharm.2024.124071.
[68] R.F. Donnelly, K. Moffatt, A.Z. Alkilani, E.M. Vicente-Pérez, J. Barry, M.T. C. McCrudden, A.D. Woolfson, Hydrogel-forming microneedle arrays can be effectively inserted in skin by self-application: a pilot study centred on pharmacist intervention and a patient information leaflet, Pharm. Res. 31 (2014) 1989–1999, https://doi.org/10.1007/s11095-014-1301-y.
[69] R.M. Lilleby Helberg, Z. Dai, L. Ansaloni, L. Deng, PVA/PVP blend polymer matrix for hosting carriers in facilitated transport membranes: synergistic enhancement of CO2 separation performance, green, Energy Environ. 5 (2020) 59–68, https://doi.org/10.1016/j.gee.2019.10.001.
[70] D. Harpaz, T. Axelrod, A.L. Yitian, E. Eltzov, R.S. Marks, A.I.Y. Tok, Dissolvable polyvinyl-alcohol film, a time-barrier to modulate sample flow in a 3D-printed holder for capillary flow paper diagnostics, Mater. Basel Switz. 12 (2019) 343, https://doi.org/10.3390/ma12030343.
[71] H. Dawud, N. Edelstein-Pardo, K. Mulamukkil, R.J. Amir, A. Abu Ammar, Hydrogel microneedles with programmed Mesophase transitions for controlled drug delivery, ACS Appl. Bio Mater. 7 (2024) 1682–1693, https://doi.org/10.1021/acsabm.3c01133.
[72] S.C. Park, M.J. Kim, S.-K. Baek, J.-H. Park, S.-O. Choi, Spray-formed layered polymer microneedles for controlled biphasic drug delivery, Polymers 11 (2019) 369, https://doi.org/10.3390/polym11020369.
[73] S. Uma Maheshwari, K. Govindan, M. Raja, A. Raja, M.B.S. Pravin, S. Vasanth Kumar, Preliminary studies of PVA/PVP blends incorporated with HAp and β-TCP bone ceramic as template for hard tissue engineering, Biomed. Mater. Eng. 28 (2017) 401–415, https://doi.org/10.3233/BME-171682.
[74] G.V. Patel, V.B. Patel, A. Pathak, S.J. Rajput, Nanosuspension of efavirenz for improved oral bioavailability: formulation optimization, in vitro, in situ and in

vivo evaluation, Drug Dev. Ind. Pharm. 40 (2014) 80–91, https://doi.org/10.3109/03639045.2012.746362.
[75] J. Andrade, C. González-Martínez, A. Chiralt, The incorporation of Carvacrol into poly (vinyl alcohol) films encapsulated in lecithin liposomes, Polymers 12 (2020) 497, https://doi.org/10.3390/polym12020497.
[76] C. Aguzzi, S. Rossi, M. Bagnasco, L. Lanata, G. Sandri, F. Bona, F. Ferrari, M. C. Bonferoni, C. Caramella, Penetration and distribution of Thiocolchicoside through human skin: comparison between a commercial foam (Miotens®) and a drug solution, AAPS PharmSciTech 9 (2008) 1185–1190, https://doi.org/10.1208/s12249-008-9162-5.
[77] X.P. Zhang, B.B. Wang, W.X. Li, W.M. Fei, Y. Cui, X.D. Guo, In vivo safety assessment, biodistribution and toxicology of polyvinyl alcohol microneedles with 160-day uninterruptedly applications in mice, Eur. J. Pharm. Biopharm. 160 (2021) 1–8, https://doi.org/10.1016/j.ejpb.2021.01.005.
[78] P. Franco, I. De Marco, The use of poly(N-vinyl pyrrolidone) in the delivery of drugs: a review, Polymers 12 (2020) 1114, https://doi.org/10.3390/polym12051114.
[79] J. Sheng, C. Liu, S. Petrovas, Y. Wan, H.-D. Chen, N.P. Seeram, H. Ma, Phenolic-enriched maple syrup extract protects human keratinocytes against hydrogen peroxide and methylglyoxal induced cytotoxicity, Dermatol. Ther. 33 (2020) e13426, https://doi.org/10.1111/dth.13426.
[80] R.S. Ray, N. Agrawal, A. Sharma, R.K. Hans, Use of L-929 cell line for phototoxicity assessment, Toxicol. Vitro Int. J. Publ. Assoc. BIBRA 22 (2008) 1775–1781, https://doi.org/10.1016/j.tiv.2008.06.015.
[81] J. López-García, M. Lehocký, P. Humpolíček, P. Sáha, HaCaT keratinocytes response on antimicrobial Atelocollagen substrates: extent of cytotoxicity, cell viability and proliferation, J. Funct. Biomater. 5 (2014) 43–57, https://doi.org/10.3390/jfb5020043.
[82] K.C. Aske, C.A. Waugh, Expanding the 3R principles: more rigour and transparency in research using animals, EMBO Rep. 18 (2017) 1490–1492, https://doi.org/10.15252/embr.201744428.
[83] O.-K. Yoo, W.J. Choi, Y.-S. Keum, Cardamonin inhibits Oxazolone-induced atopic dermatitis by the induction of NRF2 and the inhibition of Th2 cytokine production, Antioxid. Basel Switz. 9 (2020) 834, https://doi.org/10.3390/antiox9090834.
[84] P. Makvandi, M. Kirkby, A.R.J. Hutton, M. Shabani, C.K.Y. Yiu, Z. Baghbantaraghdari, R. Jamaledin, M. Carlotti, B. Mazzolai, V. Mattoli, R. F. Donnelly, Engineering microneedle patches for improved penetration: analysis, Skin Models and Factors Affecting Needle Insertion, Nano-Micro Lett. 13 (2021) 93, https://doi.org/10.1007/s40820-021-00611-9.
[85] S. Weidinger, L.A. Beck, T. Bieber, K. Kabashima, A.D. Irvine, Atopic dermatitis, Nat. Rev. Dis. Primer 4 (2018) 1, https://doi.org/10.1038/s41572-018-0001-z.
[86] A. Strzepa, C.J. Gurski, L.J. Dittel, M. Szczepanik, K.A. Pritchard, B.N. Dittel, Neutrophil-derived myeloperoxidase facilitates both the induction and elicitation phases of contact hypersensitivity, Front. Immunol. 11 (2020) 608871, https://doi.org/10.3389/fimmu.2020.608871.
[87] W. Lin, H. Chen, X. Chen, C. Guo, The roles of neutrophil-derived myeloperoxidase (MPO) in diseases: the new Progress, Antioxid. Basel Switz. 13 (2024) 132, https://doi.org/10.3390/antiox13010132.
[88] H. Niehues, G. Rikken, I.M.J.J. van Vlijmen-Willems, D. Rodijk-Olthuis, P.E.J. van Erp, P.L.J.M. Zeeuwen, J. Schalkwijk, E.H. van den Bogaard, Identification of keratinocyte mitogens: implications for Hyperproliferation in psoriasis and atopic dermatitis, JID Innov. Skin Sci. Mol. Popul. Health 2 (2022) 100066, https://doi.org/10.1016/j.xjidi.2021.100066.
[89] Y. Oishi, Z.W. Fu, Y. Ohnuki, H. Kato, T. Noguchi, Molecular basis of the alteration in skin collagen metabolism in response to in vivo dexamethasone treatment: effects on the synthesis of collagen type I and III, collagenase, and tissue inhibitors of metalloproteinases, Br. J. Dermatol. 147 (2002) 859–868, https://doi.org/10.1046/j.1365-2133.2002.04949.x.
[90] K. Pfisterer, L.E. Shaw, D. Symmank, W. Weninger, The extracellular matrix in skin inflammation and infection, Front. Cell Dev. Biol. 9 (2021) 682414, https://doi.org/10.3389/fcell.2021.682414.
[91] P. Martin, J.D. Goldstein, L. Mermoud, A. Diaz-Barreiro, G. Palmer, IL-1 family antagonists in mouse and human skin inflammation, Front. Immunol. 12 (2021) 652846, https://doi.org/10.3389/fimmu.2021.652846.
[92] Y. Cai, F. Xue, C. Quan, M. Qu, N. Liu, Y. Zhang, C. Fleming, X. Hu, H.-G. Zhang, R. Weichselbaum, Y.-X. Fu, D. Tieri, E.C. Rouchka, J. Zheng, J. Yan, A critical role of the IL-1β-IL-1R signaling pathway in skin inflammation and psoriasis pathogenesis, J. Invest. Dermatol. 139 (2019) 146–156, https://doi.org/10.1016/j.jid.2018.07.025.
[93] Z. Samochocki, J. Bogaczewicz, A. Sysa-Jędrzejowska, D.P. McCauliffe, E. Kontny, A. Wozniacka, Expression of vascular endothelial growth factor and other cytokines in atopic dermatitis, and correlation with clinical features, Int. J. Dermatol. 55 (2016) e141–e146, https://doi.org/10.1111/ijd.13132.